The Report Committee for Juan Elias Garcia
Certifies that this is the approved version of the following report:

Piezoelectric Transducer Built-in Self-Test for Logging While Drilling Instrument Sensor Evaluation at Rig Site

APPROVED BY
SUPERVISING COMMITTEE:

Nur Touba, Supervisor

Jacob Abraham

Piezoelectric Transducer Built-in Self-Test for Logging While Drilling Instrument Sensor Evaluation at Rig Site

by

Juan Elias Garcia, BSEE

Report

Presented to the Faculty of the Graduate School of

The University of Texas at Austin

in Partial Fulfillment

of the Requirements

for the Degree of

MASTER OF SCIENCE IN ENGINEERING

The University of Texas at Austin

May 2014

Dedication

This report and work is dedicated to my wife Nancy for her support and patience, and to my two boys, Maximus and Matthew.

Acknowledgements

I would like to thank Dr. Nur Touba for supervising this report and Dr. Jacob Abraham for being the reader. I would also like to thank all the instructors in the Integrated Circuits and Systems (ICS) professionals program. The ICS program is well organized, extremely challenging, and has given me a solid foundation in circuits and systems design. A special thanks to my technical advisor at Baker Hughes, Roger Steinsiek, EE, project leader, manager, for his help and guidance. While working on my MSEE at UT-Austin I have been employed at Baker Hughes and I am thankful for the support of all my previous managers and the organization.

Abstract

Piezoelectric Transducer Built-in Self-Test for Logging While Drilling Instrument Sensor Evaluation at Rig Site

Juan Elias Garcia, M.S.E.

The University of Texas at Austin, 2014

Supervisor: Nur Touba

Logging While Drilling (LWD) instruments used in oil and gas exploration are subjected to extreme environmental conditions that make reliable operation a major challenge. The sensors directly exposed to this environment experience accelerated aging and may suffer physical damage leading to failure. The cost of drilling and rig operations is very high magnifying any failures or issues with LWD tools. The goal of this report is to present a built-in self-test for an instrument sensor that provides a means to evaluate sensor functionality. The sensor is a piezoelectric ultrasonic transducer. A brief review of the sensor physics will be given. I will review some methods for characterizing piezoelectric ceramic materials and transducers. The application of sensor test methods is applied in an ultrasound pulse-echo application. A brief review of the application circuit will be covered including state of the art in commercial ultrasound integrated circuit design. A prototype of the BIST method is evaluated using test transducers to verify the circuit provides indication of a transducers ability to function correctly. The

prototype is achieved through the AD5933 demo board and MATLAB is used for data processing.

Table of Contents

List of Tables

List of Figures

Chapter 1: Introduction

Logging While Drilling (LWD) instruments used in oil and gas exploration are subjected to extreme environmental conditions which make reliable operation a major challenge. The sensors directly exposed to this environment experience accelerated aging and may suffer physical damage leading to failure. The cost of drilling and rig operations is very high magnifying any failures or issues with LWD tools. The goal of this report is to present a built-in self-test for the instrument sensor that provides a means to evaluate sensor functionality.

MOTIVATION : RELIABLE LWD

Driven by increasing demand from an emerging global middle class, oil and gas exploration continues to enter new frontiers. Innovations in exploration techniques and technology have enabled the continued growth from ultra-deep offshore drilling, to land based horizontal drilling in unconventional reservoirs. The economics justify increased spending on every aspect of the exploration and production process leading to staggering costs of daily rig rates and other essential technology.

High daily rig rates are one of the motivations for increasing investment in developing new drilling systems. Another reason for continued investment is due to the worsening operating conditions as we drill deeper. Some operating specifications of drilling system instruments can range from 150C, 20kpsi to 175C, 30kpsi and beyond for high temperature high pressure (HTHP) wells. Typically the most lucrative oil fields have the highest operating costs and the worst operating conditions for the drilling system. The sensors directly exposed to this environment experience accelerated aging and are more likely to suffer physical damage leading to failure. Extensive resources and capital is spent on reliability testing and analysis. However, it is not practical to

simultaneously test full functionality over the entire operating range and all conditions while maintaining a proper sample size for qualification. The problem is exacerbated for manufacturing tests since the production schedule and budget further limits thoroughness of testing. Therefore, a more practical approach is to design a built-in self-test to provide measurements which may be used to indicate damage or end of life, providing the opportunity to prevent a field failure, where the cost of failure would be significantly high.

ULTRASOUND APPLICATIONS

Ultrasound is simply a sound or acoustic wave we humans cannot hear. The average human hearing range is approximately 20Hz to 20 KHz. The word "acoustic" is derived from the Greek words akoustickos, meaning "of or for hearing, ready to hear" and akoustos, meaning "heard, audible". However, the scientific field of Acoustics, which deals with the study of mechanical waves, involves the study of sound above (ultrasound) and below (infrasound) the hearing range of the average person. Thus the term "acoustic wave" is often used to refer to any sound wave, whether it is infrasound, ultrasound, or an audible sound wave. The term sonic is derived from the Latin word "sonus", which means "noise, sound", thus is often used interchangeably with the word sound. This work will focus on ultrasonic sensors used in ultrasound applications such as non-destructive evaluation, or imaging.

Wave and Ultrasound Fundamentals

Ultrasound can be defined as acoustic waves propagating within a matter medium at frequencies exceeding the auditory band. An acoustic wave is a physical phenomenon during which mechanical energy is transferred through matter, without mass transfer, and which originates from a local change in the stress or pressure field within the medium

[Azhari, 2010]. In each definition above the origination and propagation of the wave occurs in a matter medium, thus acoustic waves cannot propagate in a vacuum as opposed to electromagnetic waves. The properties of the medium are of fundamental importance since they have a direct impact on the properties of the acoustic wave, such as speed of propagation and attenuation.

Wave Basics

The characteristics of a propagating wave are determined by the perturbation causing it and by the properties of the medium. Classifications of waves may be defined based on the direction of wave propagation and the motion direction of the particles constituting the medium. In a longitudinal (aka P-wave) wave the wave propagation is parallel to the motion of the medium particles. In a transverse (aka S-wave) wave the particles motion is perpendicular to the wave propagation direction.

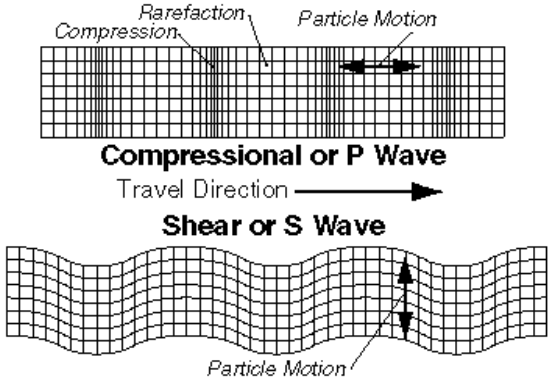

Figure 1: Longitudinal waves are also known as a P-wave particles move in the same direction as the wave. In transverse waves, also known as Shear or S-wave, particle motion is perpendicular to wave propagation direction.

There are also wave types where the motional direction of the medium particles is not fixed relative to the wave propagation, such as surface waves in which the particles move in a circular pattern. Additionally, the wave front geometry may be classified as

planar or circular. In general, waves obey the principle of superposition. When they overlap they may interfere constructively or destructively, but after they passing each other they proceed as usual.

Waves may vary with time and space, which we may define mathematically as

$$f(x,t) = f(x \pm vt) \tag{1.1}$$

for a wave in one dimension traveling in the negative (x+vt) or positive (x-vt) direction with a velocity *v*. This function may serve as a solution to the wave equation in one dimension for a scalar function *f*.

$$\frac{\partial^2 f}{\partial x^2} - \frac{1}{v^2}\frac{\partial^2 f}{\partial t^2} = 0 \tag{1.2}$$

This is no ordinary differential equation. In fact, the wave equation is a linear, second order, partial differential equation useful for the analysis of various wave phenomena. A 1D wave function traveling in the positive direction can be conveniently expressed as

$$f = Ae^{-j(\omega t - kx)} \tag{1.3}$$

or using Euler's equation,

$$f = A[\cos(\omega t - kx) + j\sin(\omega t - kx)] \tag{1.4}$$

where A is the amplitude, ω is the temporal frequency (angular frequency), and the wave number, *k,* is the spatial frequency. The wave number has units of radians per length and is related to the wavelength λ by

$$k = \frac{2\pi}{\lambda} \tag{1.5}$$

The wave velocity may be defined by the phase velocity, *v*, which may be given by

$$v = \frac{\omega}{k} \tag{1.6}$$

It should be pointed out that the wave number is the magnitude of the wave vector which, which is a vector that points in the direction of the phase velocity.

GOALS AND SCOPE OF THIS WORK

The goal of this work is to achieve a built-in self-test for a piezoelectric sensor to evaluate its functionality and prevent field failure. Additionally, this report is to provide a foundational understanding of piezoelectric transducer physics. In chapter 2 a brief but somewhat detailed review will be given for the origination of the piezoelectric effect, piezoelectric resonator, and piezoelectric ceramics. In chapter 3 a detailed review of impedance characterization and modeling of piezoelectric ceramics in the area of resonance will be given, followed by an introduction to transducer modeling just for awareness. Chapter 4 specifies a strategy to implement a built-in self-test for a ceramic piezoelectric transducer. In addition the application circuit will be introduced and a review of state of the art commercial integrated circuits is given. Chapter 5 presents the results of the circuit implementation of the BIST method.

Chapter 2: Review of Piezoelectric Sensor Physics

The "piezo" in the term Piezoelectric is derived from the Greek word piezein, which means to squeeze or press [Wikipedia]. Thus piezoelectricity[1] is the ability of a material to develop electric charge in proportion to a mechanical stress. Pierre and Jacques Curie were given credit for its discovery in 1880, following their hypothesis that electrical charge buildup on certain crystals was caused by pressure due to non-uniform heating. This is a somewhat subtle distinction from the already known pyroelectric effect, in which a direct link is made between uniform heating of a crystal and electrical charge build up. The Curie brothers demonstrated that some crystals compressed in particular directions show positive and negative charges on certain portions of their surfaces, the charges being proportional to the pressure, and disappearing when gone [Cady, 1946]. This was termed the direct piezoelectric effect. Soon after it was shown that the application of an electric field caused a proportional mechanical strain, and this was called the converse effect. To fully understand and appreciate the piezoelectric effect a brief review of various subjects will be given including solid state science, polarization theory, and crystallography.

PIEZOELECTRIC EFFECT PREREQUISITES

A crystal structure is a unique arrangement of atoms or molecules in a crystalline liquid or solid, which may be further categorized into point groups. There are 32 crystal classes or point groups into which all crystalline material may be divided. By combining the elements of symmetry of elastic tensors and of electric vectors with the geometrical symmetry of crystal elements, Woldemar Voigt made clear which of the 32 crystal classes piezoelectric effects may exist [Cady, 1946],[Voigt, 1910]. Of the 32, 21 lack a

[1] W.G.Hankel proposed the name "Piezoelectricity"

center of symmetry, and 20 of the 21 are piezoelectric. Although the cubic class 432 lacks a center of symmetry, it does not permit piezoelectricity. Ten of the piezoelectric crystalline classes are also pyroelectric, thus able to develop an electric charge when uniformly heated. These pyroelectric materials contain a unique polar axis (electric dipole moment) in the unstrained condition [Jaffe, 1971]. Further, those pyroelectric materials whose polar crystal dipole may be reversed by the application of an electric field are classified as Ferroelectric. This is summarized in the figure below. In this work we are primarily concerned with piezoelectric ceramics such as Barium Titanate, $BaTiO_3$, Lead Titanate $PbTiO_3$, and Lead Zirconium Titanate.

<table>
<tr><td colspan="4">32 Crystalline classes</td></tr>
<tr><td colspan="3">20 classes piezoelectric</td><td rowspan="3">non piezoelectric</td></tr>
<tr><td colspan="2">10 classes pyroelectric</td><td rowspan="2">non pyroelectric</td></tr>
<tr><td>ferroelectric</td><td>non ferroelectric</td></tr>
<tr><td>eg : $BaTiO_3$, $PbTiO_3$</td><td>eg : Tourmaline</td><td>eg : Quartz</td><td></td></tr>
</table>

Figure 2: There are 32 crystalline classes, of which 21 lack a center of symmetry, 20 of the 21 are piezoelectric, and of those twenty, 10 are pyroelectric [Wikipedia].

Ferroelectric materials possess a spontaneous electric polarization which may be reversed by the application of an electric field. The creation of useful piezoelectric polycrystalline material depends on ferroelectricity [Jaffe, 1971]. In the 1940s it was found, through the study of the dielectric properties of ceramic barium titanates, that it possessed a high dielectric constant, and that the cause of the high dielectric constant was ferroelectricity [Jaffe, 1971].

At this point it is prudent to re-familiarize ourselves with dielectric polarization in a capacitor resulting from the application of an electric field. The capacitance may be given from the permittivity ε, area A, and thickness t. Note that the dielectric constant K was deprecated in IEEE Std 211-1997, but will be used in this report on occasion due to its wide usage in past literature.

$$C = \frac{\varepsilon_0 K A}{t} = \frac{\varepsilon_0 \varepsilon_r A}{t} = \frac{\varepsilon A}{t} \tag{2.1}$$

Additionally, the accumulated charge, Q, is proportional to the voltage or electric field E.

$$Q = CV = \frac{\varepsilon A V}{t} = \varepsilon A E \tag{2.2}$$

The electric displacement, D, as a result of an applied field E is given below.

$$D = \frac{Q}{A} = \frac{\varepsilon V}{t} = \varepsilon E \tag{2.3}$$

The electric susceptibility χ_e, is a measure of how easily a dielectric polarizes in response to an electric field, and is related to permittivity by $\chi_e = \varepsilon_r - 1$, with polarization given by P below. Now we may also define the electric displacement in terms of polarization and electric susceptibility.

$$P = \varepsilon_0 \chi_e E \tag{2.4}$$

$$D = \varepsilon_0 E + P = \varepsilon_0 E + \varepsilon_0 \chi_e E = \varepsilon_0 \varepsilon_r E \tag{2.5}$$

Polling and Perovskite

Perovskite is a mineral known as calcium titanate or calcium titanium oxide ($CaTiO_3$). It is named after mineralogist L. A. Perovski, who discovered it in 1839 [Farndon, 2009]. Any material with the same type of crystal structure as $CaTiO_3$ is said to have a Perovskite structure. The general chemical formula is ABX_3 where A and B are

cations and X is an anion that bonds them. Most of the commercially important ferroelectric materials possess some distortion of the perovskite crystal structure, as shown in the figure below [Safari, Akdogan, 2008].

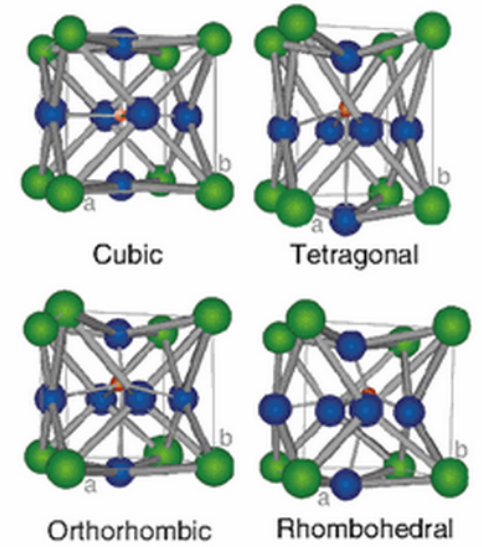

Figure 3: Cubic perovskite structure and several of the common ferroelectric distortions of the perovskite unit cell(shown for $BaTiO_3$ with exaggerated ionic displacements).

In each of the distorted unit cells it clearly shows that the center of positive and negative charge is no longer coincides, thus providing a foundation for spontaneous polarization (P_s). Note that the distorted structures expand parallel to the polarization, and contract perpendicular to it. This correlates mechanical strain to polarization in the lattice, underlies the importance of crystallographic orientation and helps visualize the underlying structure leading to anisotropic behavior. The crystallographic symmetry of Tetragonal, Orthorhombic, and Rhombohedral correspond to a polar axis of [001], [110], and [111], respectively. Often the crystal class/point groups may be described in terms of the Hermann-Mauguin symbol system which correlates to 4mm for tetragonal, 3m for rhombohedral and mm2 for orthorhombic [Jaffe, Cook, Jaffe, 1971]. A table

summarizing some of the relationships can be found in reference [Safari, Akdogan, 2008].

Perovskite electro-ceramics are used in many applications such as multilayer ceramic capacitors (MLCC), and piezoelectric transducers. A significant step leading to the commercialization of piezoelectric ceramics is the development of a "poling" process to achieve ferroelectric distortions of the perovskite structure. This process was first clearly recognized and patented by R. B. Gray of the Erie Resistor Company in September of 1946 [Jaffe, Cook, Jaffe, 1971]. The following polling process described below is summarized from the technical brochure of APC International, LTD., formerly American Piezo Ceramics Inc. Starting with fine powders of the component metal oxides a piezoelectric ceramic may be formed and fired to a desired shape. During this process the material attains a dense crystalline structure, and receives electrodes after cooling. A fired ceramic element is a semi-organized mass of fine crystallites (ceramic grains). Above the Curie point, each perovskite crystal exhibits a simple cubic symmetry with no dipole moment. At temperatures below the Curie point each crystal exhibits tetragonal or rhombohedral symmetry and its structure carries a dipole moment. The dipole moments are orientated differently among different ceramic grains or regions. Domains are regions where the dipoles are like-oriented, but the domains are organized randomly so there is no net polarization. The ceramic is polarized (poled) by exposing it to a strong, direct current (DC) electric field, usually, but not exclusively at a temperature slightly below the Curie point. When the field is removed most of the dipoles are locked in place and a permanent polarization and a permanent deformation (elongation) remain.[APC, 2011]

Lead Zirconate Titanate (PZT)

Lead zirconate, $PbZrO_3$, is antiferroelectric (therefore not piezoelectric), and pure $PbTiO_3$ by itself is of limited interest as a piezoelectric material because of the difficulties associated with its creation and measure [Safari, Akdogan, 2008]. However, it is interesting that a solid solution of these two compositions, $Pb(Zr_{1-x}Ti_x)O_3$, aka PZT, exhibits outstanding piezoelectric properties. It has been determined that lead zirconate titanate materials exhibit greater sensitivity and higher operating temperatures relative to barium titanate, thus PZT has replaced $BaTiO_3$ materials in many applications and has become the most widely used piezoelectric ceramic [APC, 2011]. Shown below is a phase diagram for PZT solid solution perovskite system [Safari, Akdogan, 2008].

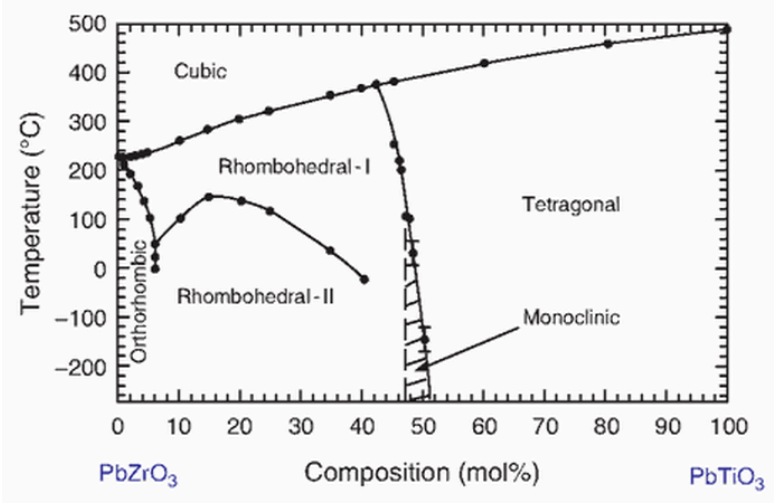

Figure 4: PZT phase diagram

> *Safari, Akdogan, 2008*: For Ti concentrations above about 48 mol% the material adopts a tetragonally distorted ferroelectric phase. At the morphotropic phase boundary (MPB, the nearly temperature-independent boundary between the two ferroelectric distortions), there is a transition to the rhombohedral distortion, with a sliver of monoclinic phase that appears at low temperatures.

Another interesting phase diagram for PZT is shown below [Safari, Akdogan, 2008].

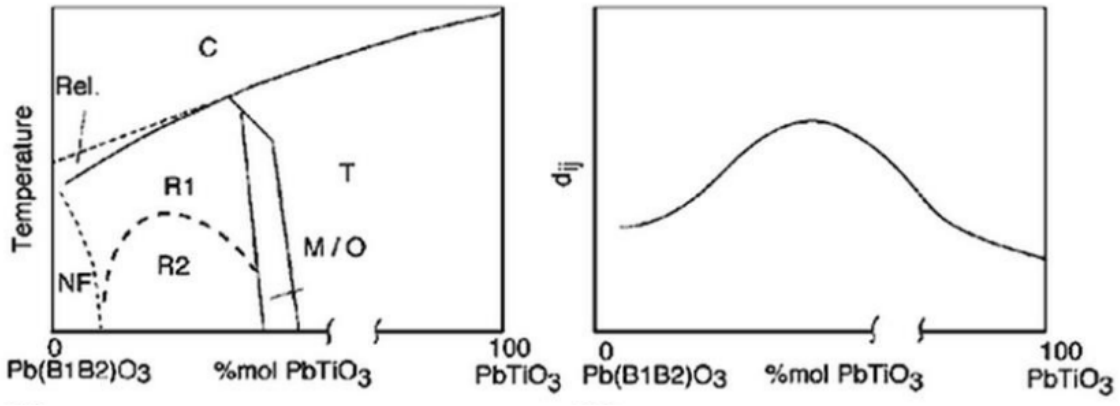

Figure 5: Simplified PZT or PbTiO3-relaxor ferroelectrics phase diagram (left) and a schematic illustration of the variation in piezoelectric charge constant d (right).

Safari, Akdogan, 2008: For PZT, B1=B2=Zr. T is tetragonal phase, M/O is a monoclinic or orthorhombic phase, R1 and R2 are rhombohedral phases differing in rotation of oxygen octahedral, NF is either relaxor or antiferroelectric phase, and Rel. is a relaxor phase. In PZT, relaxor phase is absent and NF phase is antiferroelectric. For details see (Woodward et al. 2005, Jaffe et al. 1971, Eitel and Randall 2007, Noheda et al. 1999)

Comparing the two graphs in figure 5, it is interesting to note that the maximum of the piezoelectric effect coincides with the morphotropic phase boundary.

PIEZOELECTRIC CHARACTERIZATION PARMETERS

Possibly the best single measurement of the strength of a piezoelectric effect is the electromechanical coupling factor k, which measures the fraction of electrical energy converted to mechanical energy (or vice versa when a piezoelectric crystal or ceramic is stressed) [Jaffe, Cook, Jaffe, 1971].

$$k^2 = \frac{electrical\ energy\ converted\ to\ mechanical\ energy}{input\ electrical\ energy}$$

or

$$k^2 = \frac{mechanical\ energy\ converted\ to\ electrical\ energy}{input\ mechancial\ energy}$$

This electromechanical energy conversion makes piezoelectric materials extraordinary, since stress (T) applied to ordinary solids will simply cause a proportional strain (S) multiplied the material constant for elasticity, Y, Young's modulus.

$$T = YS \tag{2.6}$$

The "direct" piezoelectric effect refers to the creation of electrical charge due to a mechanical stress, and the "converse" effect is when an electric field (E) produces a proportional strain. This can be described as follows, where the electrical charge is given in terms of electric displacement (D), and introducing a piezoelectric constant of proportionality *d* (piezoelectric charge constant).

$$D = Q/A = dT \tag{2.7}$$

$$S = dE \tag{2.8}$$

$$d = D/T = S/E \tag{2.9}$$

The constant *d* is numerically identical for both effects, but the units are necessarily different, given by coulombs/Newton and meter/Volt for the direct and converse effect respectively. The piezoelectric constant *g*, which gives the field produced by a stress is related to the *d* constant by the permittivity [Jaffe, Cook, Jaffe, 1971].

$$g = \frac{d}{\varepsilon'} = \frac{d}{K\varepsilon_0} \tag{2.10}$$

Additionally the piezoelectric constant *e* relates stress *T* to field *E*, and *h* relates strain *S* to field *E*.

Since piezoelectric ceramics are anisotropic, their physical constants must take into account the direction of the applied electric and mechanical forces in addition to boundary conditions. This typically results in the constants having a superscript

describing the boundary condition, and one or two subscripts describing the direction of the forces affecting the piezoelectric element. As shown in the figure below, the subscripts 1, 2, or 3 corresponds to X, Y, Z, respectively, and shear about one of these axes is represented by 4, 5, 6, respectively [APC, 2011]. The direction of polarization is usually made to coincide with the Z-axis.

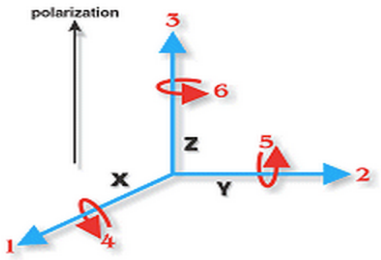

Figure 6: Directions of forces affecting a piezoelectric element.

There are additional subscripts used to indicate certain conditions such as "p" signifying that the stress is equal in all directions perpendicular to the direction 3 (Z-axis) and that the electrodes are on the faces perpendicular to the Z-axis. The subscript "h" means the stress is hydrostatic in nature. The boundary conditions, when applicable, are indicated by the superscript and are summarized in the table below.

Superscript	Condition
T	Constant stress (mechanically free)
S	Constant strain (mechanically constrained)
D	Constant electrical displacement (open circuit)
E	Constant field (short circuit)

Table 1: Superscripts of Piezoelectric constants indicating the boundary condition during the measurement of the constant.

A few constants with superscripts and subscripts are shown in tables 2 through 6 below [APC, 2011].

ε^{T}_{11}	permittivity for dielectric displacement and electric field in direction 1 (perpendicular to direction in which ceramic element is polarized), under constant stress
ε^{S}_{33}	permittivity for dielectric displacement and electric field in direction 3 (parallel to direction in which ceramic element is polarized), under constant strain

Table 2: Permittivity

s^{E}_{11}	elastic compliance for stress in direction 1 (perpendicular to direction in which ceramic element is polarized) and accompanying strain in direction 1, under constant electric field (short circuit)
s^{D}_{33}	elastic compliance for stress in direction 3 (parallel to direction in which ceramic element is polarized) and accompanying strain in direction 3, under constant electric displacement (open circuit)

Table 3: Elastic compliance

d_{33}	induced polarization in direction 3 (parallel to direction in which ceramic element is polarized) per unit stress applied in direction 3 **OR,** induced strain in direction 3 per unit electric field applied in direction 3
d31	induced polarization in direction 3 (parallel to direction in which ceramic element is polarized) per unit stress applied in direction 1 (perpendicular to direction in which ceramic element is polarized) OR, induced strain in direction 1 per unit electric field applied in direction 3
d15	induced polarization in direction 1 (perpendicular to direction in which ceramic element is polarized) per unit shear stress applied about direction 2 (direction 2 perpendicular to direction in which ceramic element is polarized) OR, induced shear strain about direction 2 per unit electric field applied in direction 1

Table 4: Piezoelectric charge constant

g_{33}	induced electric field in direction 3 (parallel to direction in which ceramic element is polarized) per unit stress applied in direction 3 **or** induced strain in direction 3 per unit electric displacement applied in direction 3
g_{31}	induced electric field in direction 3 (parallel to direction in which ceramic element is polarized) per unit stress applied in direction 1 (perpendicular to direction in which ceramic element is polarized) **or** induced strain in direction 1 per unit electric displacement applied in direction 3
g_{15}	induced electric field in direction 1 (perpendicular to direction in which ceramic element is polarized) per unit shear stress applied about direction 2 (direction 2 perpendicular to direction in which ceramic element is polarized) **or** induced shear strain about direction 2 per unit electric displacement applied in direction 1

Table 5: Piezoelectric voltage constant

k_{33}	factor for electric field in direction 3 (parallel to direction in which ceramic element is polarized) and longitudinal vibrations in direction 3 (ceramic rod, length >10x diameter)
k_t	factor for electric field in direction 3 and vibrations in direction 3 (thin disc, surface dimensions large relative to thickness; $k_t < k_{33}$)
k_{31}	factor for electric field in direction 3 (parallel to direction in which ceramic element is polarized) and longitudinal vibrations in direction 1 (perpendicular to direction in which ceramic element is polarized) (ceramic rod)
k_p	factor for electric field in direction 3 (parallel to direction in which ceramic element is polarized) and radial vibrations in direction 1 and direction 2 (both perpendicular to direction in which ceramic element is polarized) (thin disc)

Table 6: Piezoelectric electromechanical coupling factor

Chapter 3: Methods for Characterizing Piezoelectric Transducers

For the characterization of piezoelectric transducers measuring and modeling go hand in hand due to the complexity of the piezoelectric ceramic. That is, the properties of a piezoelectric ceramic are defined by the dielectric, piezoelectric, and elastic coefficients covered in the previous chapter. In this chapter impedance measurement techniques will be reviewed along with the Butterworth Van-Dyke (BVD) circuit model valid at frequencies near resonance. Since the BVD model is only valid in the area of resonance, a review of SPICE models capable of modeling the complete transducer performance is also reviewed.

RESONANT CIRCUIT MODELS

Resonance occurs when energy is transformed in a system from one form to another periodically, i.e. the magnetic field of an inductor to the electric field of a capacitor in an LC circuit. The phenomena of resonance may be used to multiply the effect of an applied force to a system, by applying the force in tune with the resonant frequency. In a real world system there are losses that occur in the system that cause dissipation of the circulating energy, i.e. damping. Damping is an influence within or upon an oscillatory system that has the effect of reducing, restricting, or preventing its oscillations [Wikipedia]. The damping mechanism that dissipates energy stored in the oscillation is determined by the physical system. For example in an electrical system resistance would be the damping mechanism, and viscous drag for a mechanical system.

Butterworth, Van Dyke, Cady

In 1915 S. Butterworth showed theoretically that any mechanical vibrating system could be represented as an LCR branch in parallel with a capacitance [Butterworth, 1915]. Van Dyke separately arrived at the same circuit specifically for the purpose of

describing the piezoelectric and mechanical behavior of a quartz resonator [Van Dyke, 1928]. The work of Van Dyke was built on that of W.G. Cady who was a pioneer in the field of piezoelectricity and the quartz crystal resonator. The piezoelectric BVD circuit model shown below.

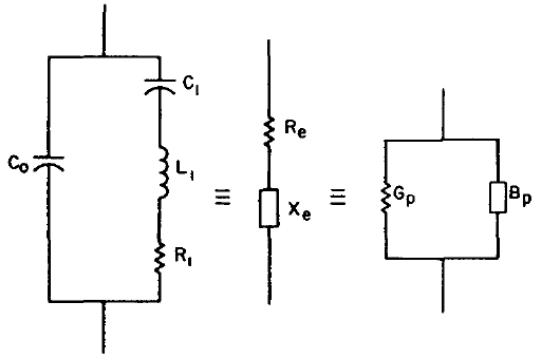

Figure 7: The Butterworth Van Dyke equivalent circuit of a quartz crystal resonator for one resonance [ieee 177, 1966].

The LCR branch represents the piezoelectric physical attributes of mass, elastic compliance, and mechanical dampening. C_0 is the capacitance in the absence of mechanical deformation. The BVD equivalent circuit model is only useful if the four circuit parameters are constant and independent of frequency and amplitude [IRE 1957]. Thus there must be no other mode of motion is near the resonance of interest, and the amplitude of vibration must be negligibly small [IRE 1957]. The reactance of a piezoelectric resonator compared to a capacitor is shown below, provided by Jaffe et. al. 1971.

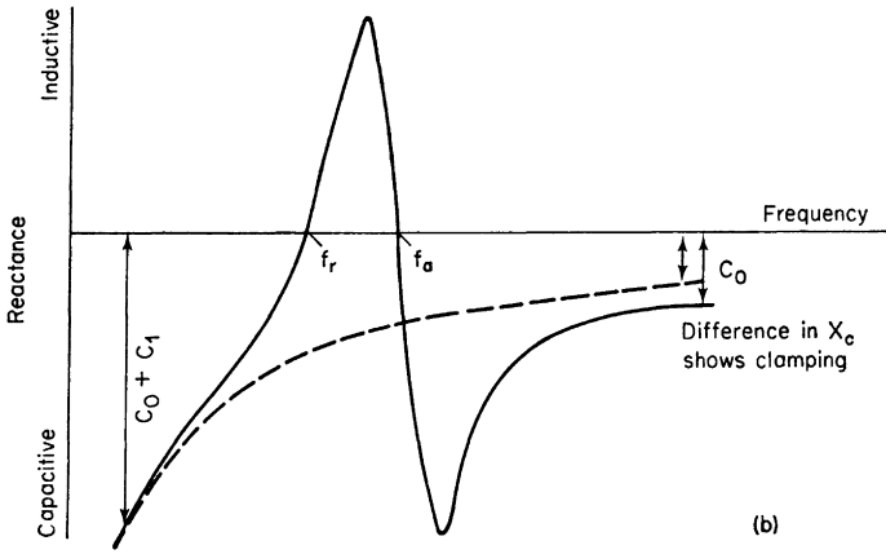

Figure 8: Reactance of a piezoelectric resonator compared with a capacitor of equal value at low frequency (dotted curve).

At lower frequencies the piezoelectric elastic effect (C_1) makes a contribution to the measured capacitance, thus is a measurement of the free dielectric constant K^T. Above all elastic resonance frequencies and their major harmonics, one observes the clamped constant K^S, and thus ceramic capacitance free of the piezoelectric effect which is blocked by inertia [Jaffe et al., 1971]. It is noted that in conjunction with K measurements the dissipation factor measurement should be taken to account for the non-idealities of the ceramic element. The challenge remains in defining the measurements and methods used to find the parameters of interest for our BVD model.

Impedance and Admittance Curves

The four fundamental parameters defined by the BVD model may be used in calculations to provide sufficient characterization of the piezoelectric transducer. This may be achieved using impedance data like that derived from a 4294B Agilent

Impedance analyzer. Shown below are impedance curves as a function of frequency, with the characteristic frequencies notated, and defined in the table below.

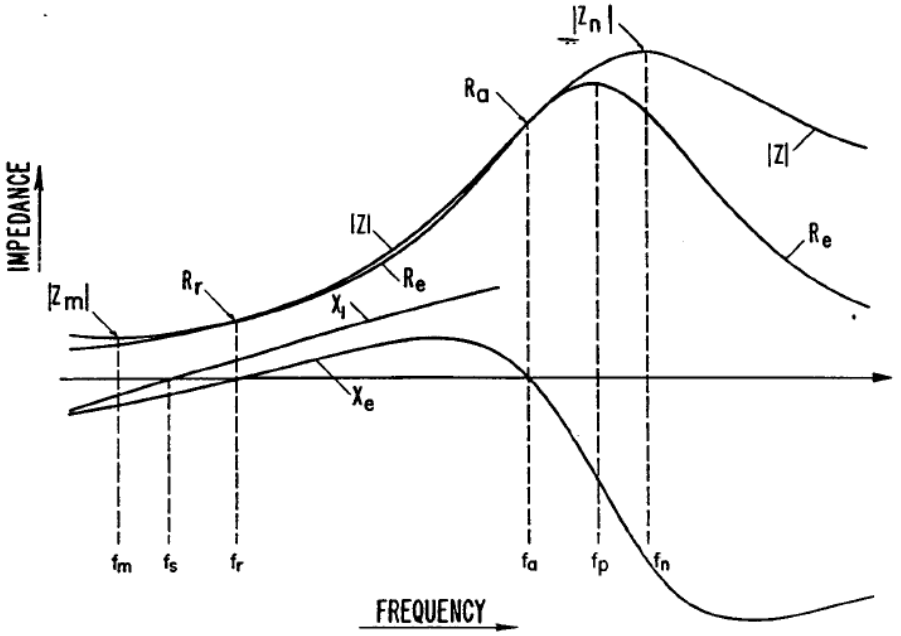

Figure 9: Impedance curves as a function of frequency, with the characteristic frequencies notated [ieee177, 1966].

f_m	Frequency at Maximum Admittance (Minimum Impedance, Z_m)
f_s	Motional (Series) Resonance frequency = $\frac{1}{2\pi\sqrt{L_1 C_1}}$
f_r	Resonance Frequency (Reactance X_e=0)
f_a	Antiresonance Frequency (Reactance X_e=0)
f_p	Parallel Resonance Frequency = $\frac{1}{2\pi}\sqrt{\frac{1}{L_1 C_1}\left(1+\frac{1}{r}\right)}$
f_n	Frequency at Minimum Admittance (Maximum Impedance)

Table 7: Characteristic Frequency parameters of the equivalent circuit [IRE 1957].

The validity of the circuit representation of the impedance or admittance of a piezoelectric vibrator is valid only if the admittance diagram circle diameter is large in comparison with the change of ωC_0 in the resonance range, or if $r \ll Q^2$ [IRE 1957]. The mechanical quality factor Q is obtained from determination of the minimum impedance Z_m, and is given by the equation below [IRE 1961].

$$Q = \frac{{f_p}^2}{2\pi f_s |Z_m| (C_o + C_1)\left({f_p}^2 - {f_s}^2\right)} \tag{3.1}$$

The capacitance ratio is r.

$$r = \frac{C_0}{C_1} \tag{3.2}$$

The separation between parallel and series resonance frequencies is given by

$$\frac{{f_p}^2 - {f_s}^2}{{f_p}^2} = \frac{C_1}{C_o} = \frac{1}{r} \tag{3.3}$$

The circle plots for Impedance and Admittance are shown below.

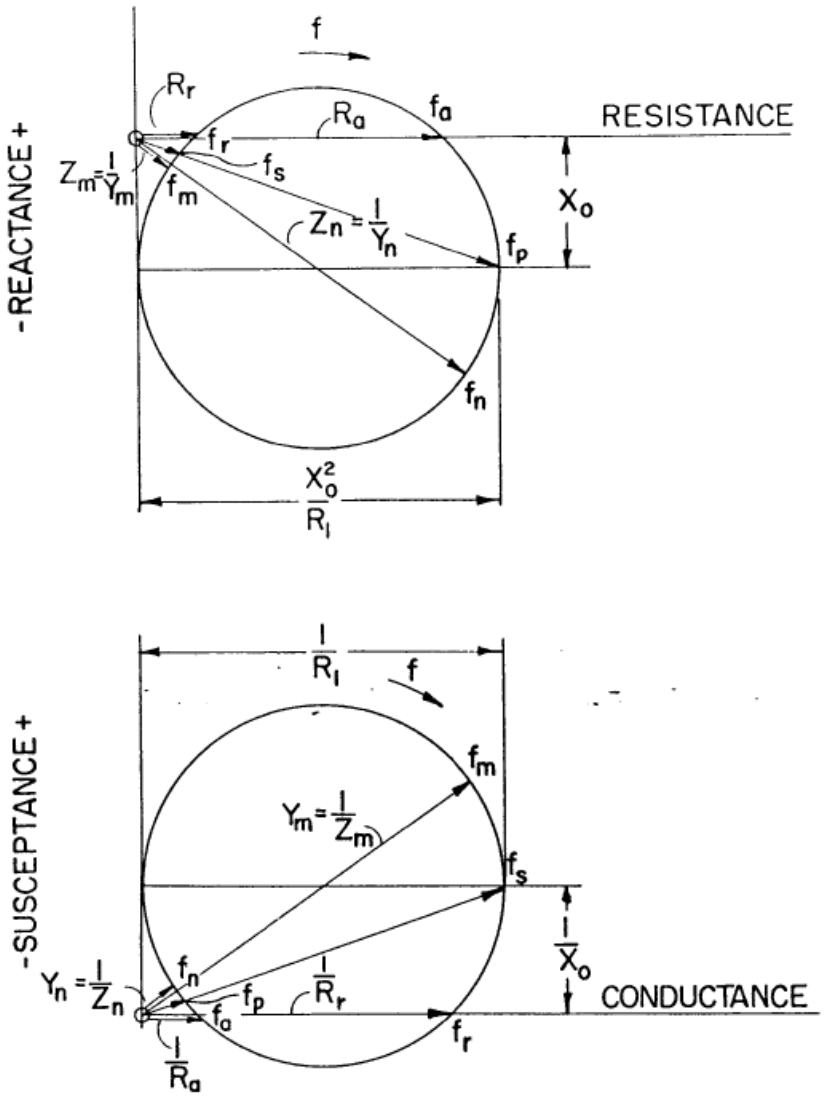

Figure 10: The impedance and Admittance diagram of a piezoelectric vibrator [ieee177, 1966].

Loaded PZT Patch "Easy Model"

The shortcomings of the BVD model have been stated and well documented in the IRE standards. Thus, research for various piezoelectric ceramic applications is focused on modifying and building on the BVD model. A growing field for piezoelectric ceramics is in structural health monitoring and for use as a smart material. The piezoelectric ceramic may be integrated into a structure for monitoring, and provides electrical signals in response to changes in the mechanical structure. In the work by [Kim, Grisso, Kim, Ha, Inman, 2008] they propose an equivalent circuit model for a PZT patch for a loaded and unloaded case. In this work they build off and extend the BVD model, Sherrit Model [Sherrit et. Al.] and the Guan model [Guan, Liao] to create an "Easy Model" for the unloaded and loaded conditions for their PZT patch.

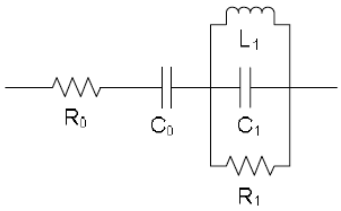

Figure 11: The "Easy Model" of an unloaded PZT patch transducer [Kim et. Al., 2008].

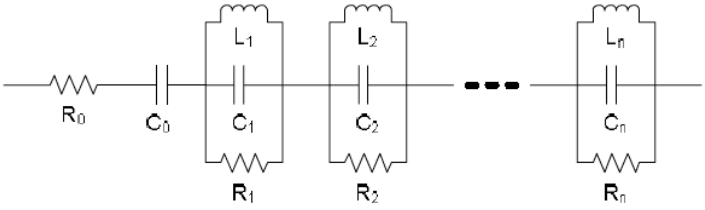

Figure 12: The "Easy Model" of a loaded PZT patch transducer [Kim et. Al., 2008].

The models were derived by measuring the impedance of the transducers over the frequency band of interest and applying the concepts introduced in the previous section.

Below are the impedance curves showing the correlation between the measurement and model [Kim, Grisso, Kim, Ha, Inman, 2008]. A series resonance can be observed at 45kHz, a parallel at 55kHz, and is inductive between. The parallel RLC was chosen because of the clear parallel resonance frequency. Series resistance R0 can be seen on non-resonant portions of resistance plot, and series capacitance from the low frequency portion of reactance curve.

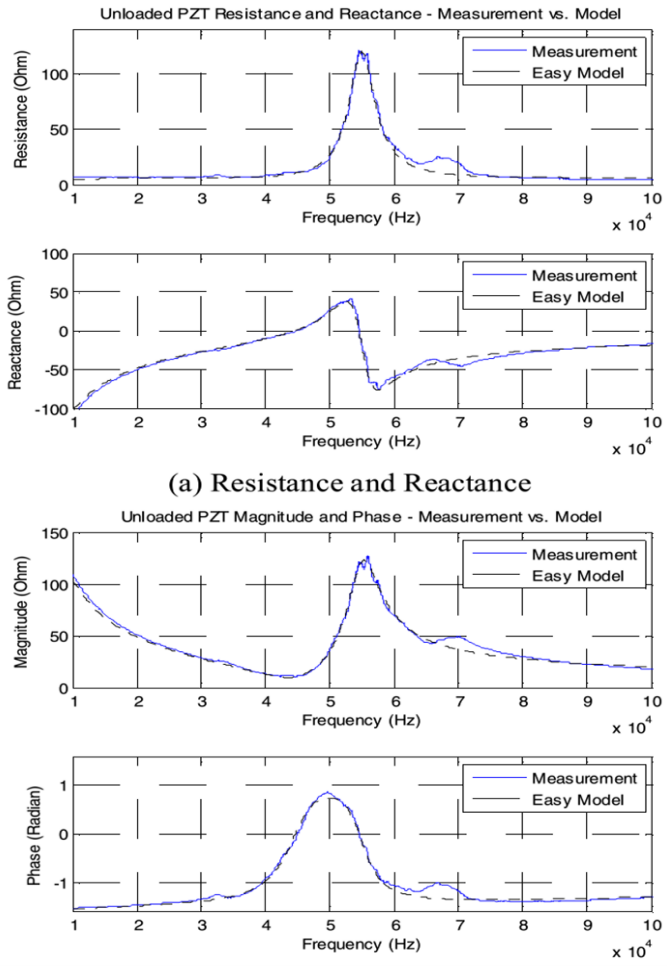

Figure 13: Model vs Measurement of the "Easy Model" of an unloaded PZT patch transducer [Kim et. Al., 2008].

Resonant Impedance Curve fitting

Reviewed below is the work by [Kwok, Chan, Choy, 1997], in which five different methods are reviewed which fit impedance resonance data to a theoretical expression for impedance. Using these methods they are able to calculate the elastic, dielectric, and piezoelectric material constants with reasonably good accuracy abiding by the method conditions. The electrical impedance at "thickness-extensional resonance" of a transducer poled in the thickness direction, lateral dimensions large compared with its thickness, and with lossless transducer plate of thickness L and electrode area A is given as,

$$Z(f) = \frac{L}{j2\pi f \varepsilon_{33}^{S} A}\left[1 - {k_t}^2 \frac{\tan\left(\pi f L \sqrt{\frac{\rho}{c_{33}^{D}}}\right)}{\pi f L \sqrt{\frac{\rho}{c_{33}^{D}}}}\right] \tag{3.4}$$

where

$${k_t}^2 = \frac{e_{33}^2}{\varepsilon_{33}^{S} c_{33}^{D}} \tag{3.5}$$

$$c_{33}^{D} = \frac{c_{33}^{E}}{1 - k_t^2} \tag{3.6}$$

ε_{33}^{S} is the clamped permittivity, k_t is the electromechanical coupling constant for the thickness mode, c_{33}^{D} is the elastic stiffness constant at constant electric displacement, c_{33}^{E} is the elastic stiffness and constant electric field, ρ is the density, and f is the frequency. It is necessary to treat certain parameters as complex quantities (i.e. c_{33}^{D*}, ε_{33}^{S*}, k_t^*), indicated by adding an asterisk, to account for the losses. The complex quantities are assumed to be independent of frequency, thus to calculate impedance only three different frequencies are required.

Largely based on [IEEE 176-1987], It is given that c_{33}^{D}, and k_t, can be determined by the following equations.

$$c_{33}^{D} = 4\rho L^2 f_p^2 \tag{3.7}$$

$$k_t^2 = \frac{\pi}{2}\frac{f_s}{f_p}\tan\left(\frac{\pi}{2}\frac{f_p - f_s}{f_p}\right) \tag{3.8}$$

The parallel and series resonant frequencies are where the real parts of impedance and admittance have a maximum respectively. For low loss materials$f_p \sim f_n$, and $f_s \sim f_m$, and thus the approximations are made that they are equal. Citing the work of [Sherrit et al., 1992], Kwok et al. applies the following equations for complex parallel and series resonance frequencies

$$f_p^* = f_p\left[1 - j\frac{f_{-1/2}^{p} - f_{+1/2}^{p}}{f_p}\right]^{-1/2} \tag{3.9}$$

$$f_s^* = f_s\left[1 - j\frac{f_{-1/2}^{s} - f_{+1/2}^{s}}{f_s}\right]^{-1/2} \tag{3.10}$$

to equations 3.7 and 3.8 above to calculate the complex material constants c_{33}^{D*}, k_t^*. The frequencies are obtained from the admittance and impedance circle plots as shown below [Kwok et al., 1997], [Sherrit et al. 1992].

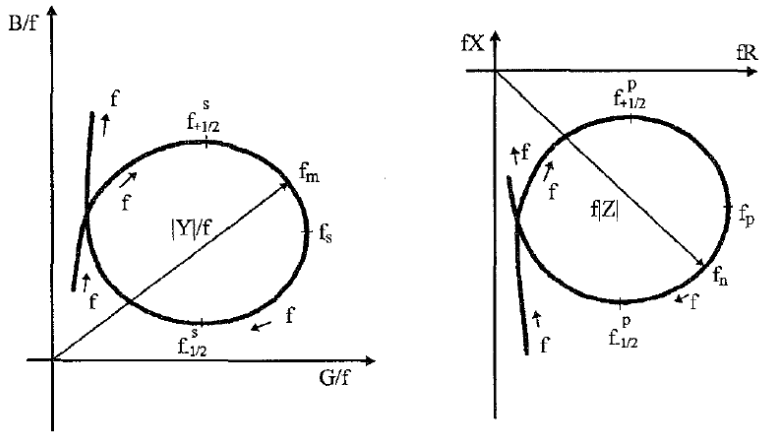

Figure 14: admittance and impedance circle plots defining complex frequencies.

Then ε_{33}^{S*} is calculated by substituting the calculated c_{33}^{D*}, and k_t^*, and the observed Z value at the frequency $2f_p$ in equation 3.4.

Smits' method [Smits, 1976] is an iterative process for calculating real and imaginary parts of the material constants that starts with an initial approximation of c_{33}^{D*}, which is observed at two frequencies near resonance, which are then substituted into (3.4) to calculate ε_{33}^{S*}, and k_t^*, which are then combined with an observed Z(f) at a third frequency to achieved an improved c_{33}^{D*}. Kwok et al. found in the review of Smits' method found that not any three Z(f) data points will converge, and when they do the method is still sensitive to the initial c_{33}^{D*}. The method used by the piezoelectric resonance program (PRAP) from TASI-Technical Software, utilizes a combination of the methods by Smits and Sherrit et al. This program uses measured impedance data to automatically find f_p, which is used as one of the three data points for the calculation which leads to a more accurate initial c_{33}^{D*} than that of the Smits' method. Kwok et al. used a nonlinear regression procedure, the Gauss-Newton method to best-fit experimental data to a nonlinear equation. The stated advantage of the nonlinear regression method is is that an arbitrary choice of data points is not necessary and that all the impedance data

points within a certain frequency range are given a best fit to the theoretical expression for the impedance to give mater parameters [Kwok et al., 1997].

Piezoelectric Transducer Self-Diagnosis Indices

In the work by [Lee and Sohn, 2010], they propose a method for self diagnoses of a PZT transducer, which consists of two self-diagnostic indices, which allow debonded and cracked transducers to be identified and distinguished from changing environmental and structural conditions. This work builds upon [Lee, Sohn, Hong, June 2010], the time reversal based piezoelectric transducer self-diagnosis under varying temperature. Shown below is a block diagram of the time reversal-based transducer debonding detection, which consists four steps.

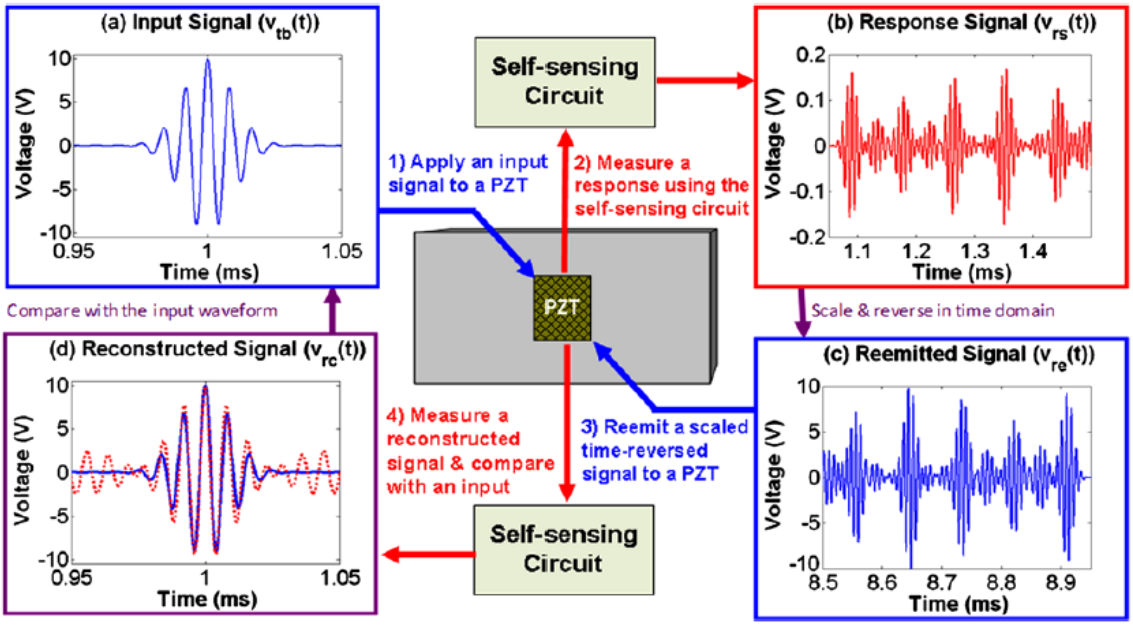

Figure 15: block diagram of the time reversal-based transducer debonding detection.

Shown below is an illustration of the detection method of a cracked PZT transducer.

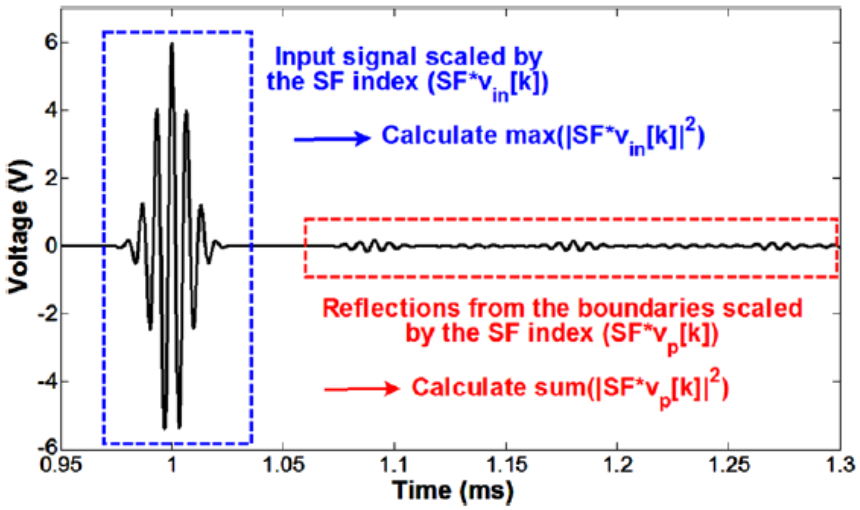

Figure 16: illustration of the detection method of a cracked PZT transducer.

TRANSDUCER CIRCUIT MODELS

The subject of piezoelectric transducer characterization and modeling would not be complete with some mention of the Mason model. Mason presented an exact equivalent circuit of the piezoelectric resonator valid over the entire frequency range as opposed to just a single area of resonance. The Mason model consisted of and electrical port and two acoustic ports through the use of an ideal electromechanical transformer. Redwood adapted the Mason model by showing the negative capacitance at the input port could be transferred to the acoustic side of the transformer and treated like a length of the acoustic line [Sherrit-1999],[Redwood, 1961]. Kirmholtz, Leedom and Mattheal [KLM-1970] published an alternative equivalent circuit in an effort to remove the circuit elements between the top of the transformer and the node of the acoustic transmission line, and is shown below in comparison to the Mason model.

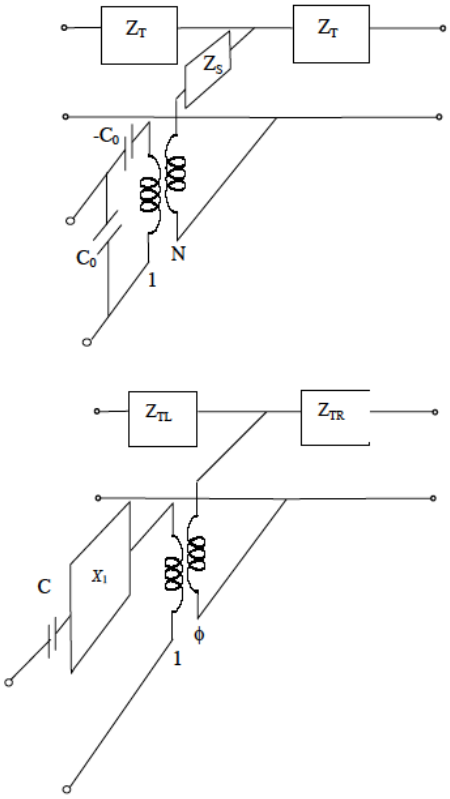

Figure 17: KLM (lower) and Mason's (upper) piezoelectric resonator equivalent circuits [Sherrit-1999].

In the work by Galliere, Papet, Latorre – 2007, noting that present transducer models only take into account one operation mode, i.e. thickness or planar, they propose a unified electrical model which will take into account both modes of operation simultaneously. The unified model is shown below.

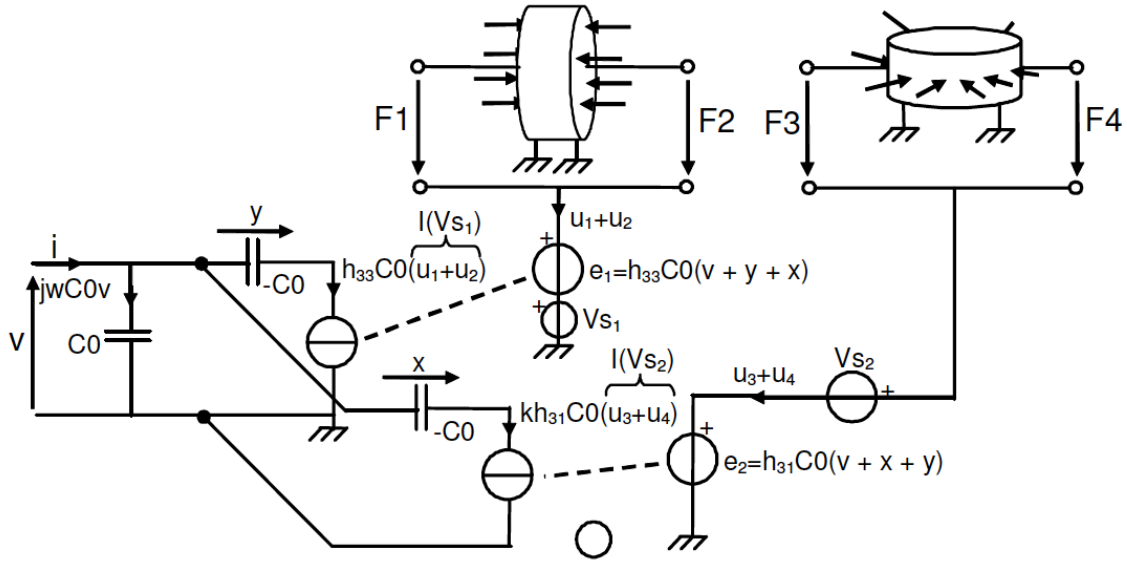

Figure 18: Unified Electrical Model for Piezoelectric Transducers.

Chapter 4: Sensor Characterization Built-in Self-Test (BIST)

In this chapter a brief review of an ultrasound application circuit will be given, with along with state of the art in commercialized integrated circuit design, and a simplified circuit for implementation. Built-in self-test circuits will be proposed to use in conjunction with a transducer and ultrasound circuit. The main objective of the sensor built-in self-test is provide a means to verify if its functionality in situ, and prevent failures in the field. Secondarily it will also provide an efficient and cost effective method for manufacturing and maintenance testing. One of the challenges is making the sensor test effective and built-in so that it may be easily performed on the rig site. The field maintenance shops and oil rigs have limited test equipment, thus it is not practical to have a sophisticated test set up. A typical oil rig is shown below.

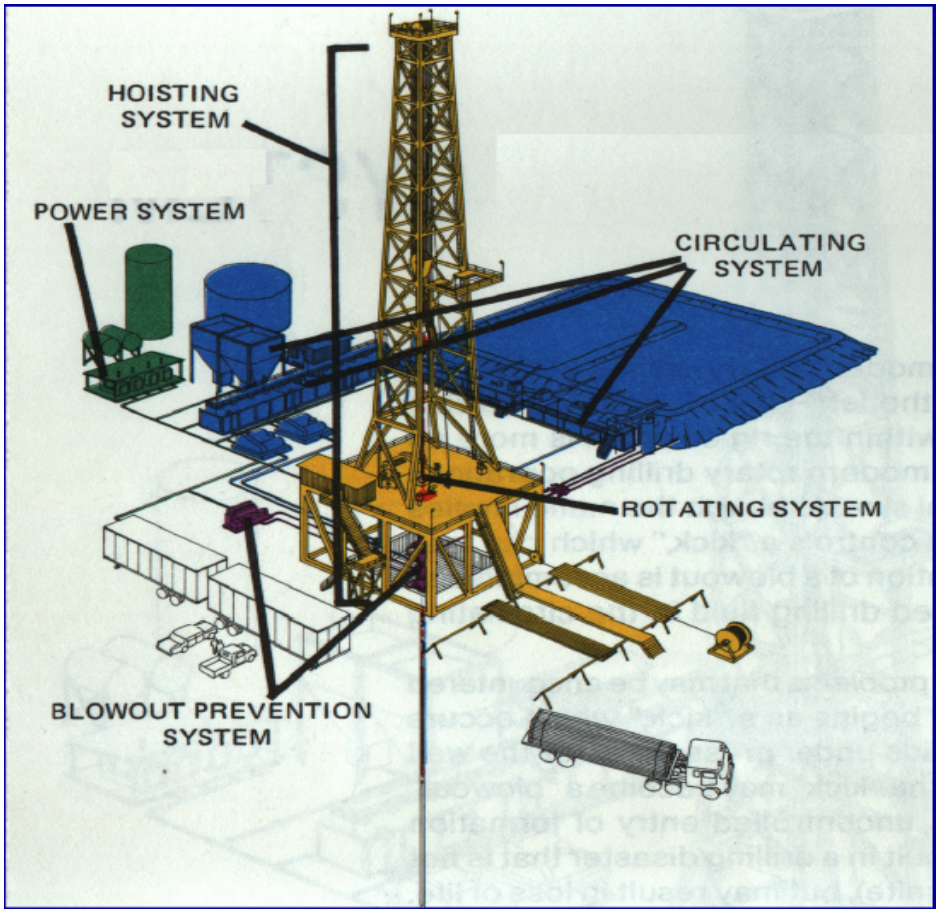

Figure 19: Typical oil rig setup [Hyne, 2012].

ULTRASOUND APPLICATION CIRCUIT

A simplified ultrasound circuit may consist of a transmitter (pulser), Receiver, transmit/receive (T/R) switches, and optionally a multiplexor to interface multiple sensors. The high voltage pulser contains power switches to apply the excitation energy to the sensor. The T/R switch in green is intended to isolate the low voltage receiver from the high-energy pulse during Transmission. The T/R switch in blue is intended to isolate the high voltage pulser from the receiver during reception of the low voltage

electrical signal from the transducer. When a multiplexor is required it must be able to handle the high energy pulses for transmission and provide a linear path for the low voltage signals received.

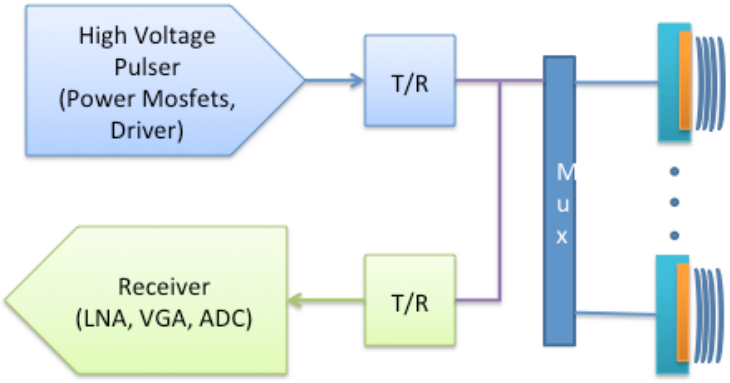

Figure 20: Simplified ultrasound circuit block diagram.

Not shown are the ultrasound optimization circuits and other peripheral circuits such as the low and high voltage power supplies. The high voltage power supplies can range from 100V to the kilo-volt range, and may be of single or dual polarity. State of the art ultrasounds ICs are becoming increasingly integrated such as Pulser MAX14808, Receiver MAX2079, and outdoing both is Transceiver MAX2082 by Maxim Integrated. A bock diagram (solid lines) of the Transceiver is shown below since the datasheet is not yet available.

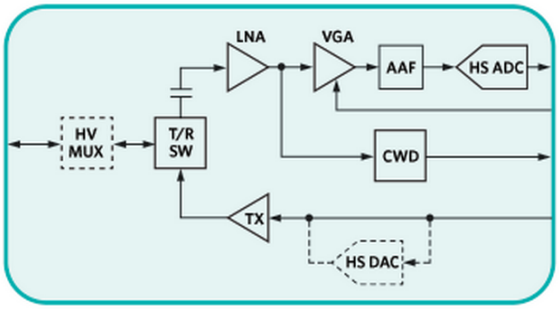

Figure 21: Simplified ultrasound circuit block diagram.

The maxim chip MAX14808 has the ability to drive 8 channels, with dual polarity up to +/-105V, return to zero (RTZ) functionality, blocking diodes, T/R switches, and damping. A functional diagram of the IC is shown below.

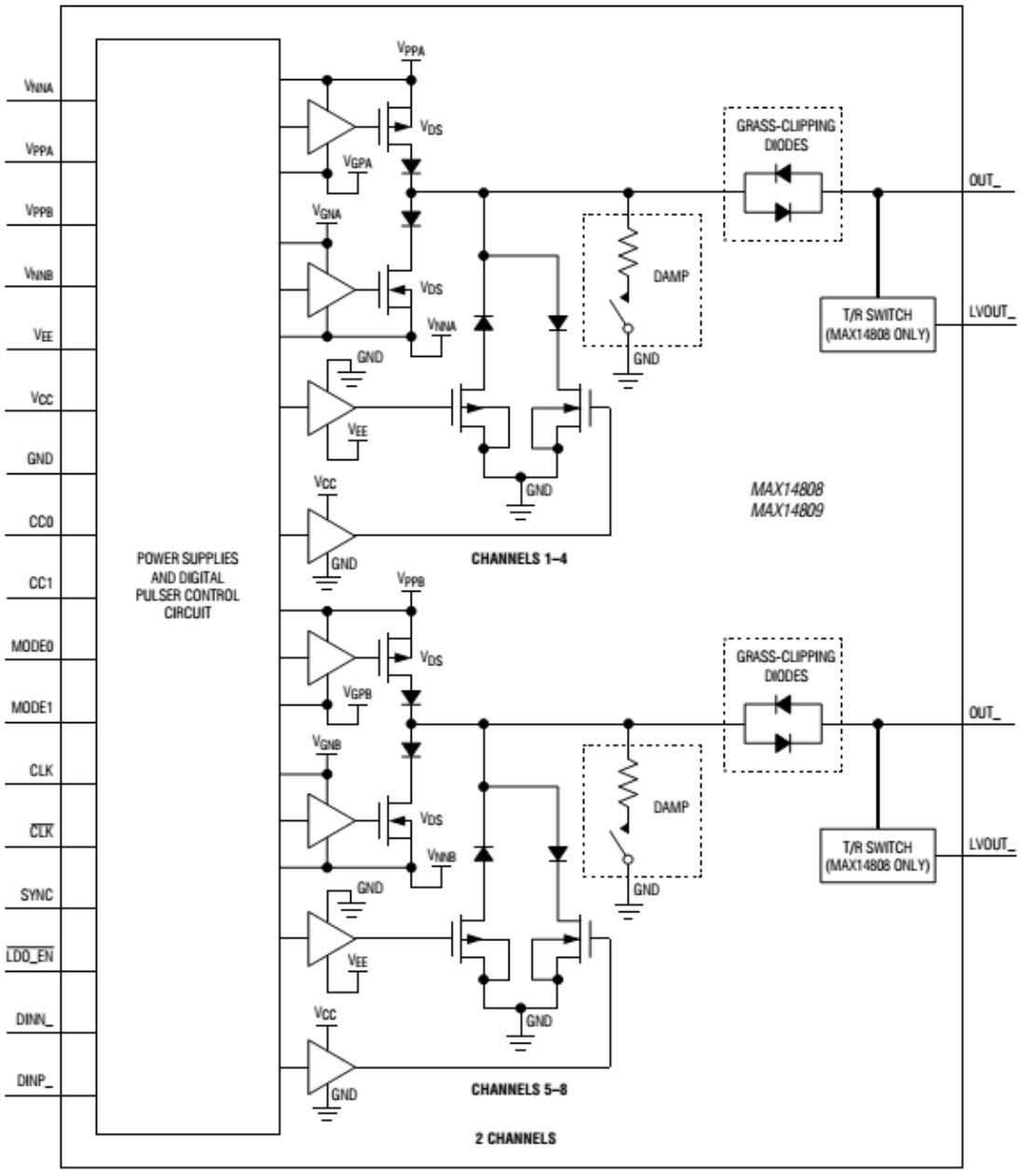

Figure 22: Simplified ultrasound circuit block diagram of MAX14808.

Supertex, who was recently bought out by Microchip, offers a competitive selection of ultrasound ICs. For simplicity I chose one of their less integrated options to implement the ultrasound pulser circuit. Shown below is a functional diagram of the circuit implementing MD1213 and TC6320 by Supertex.

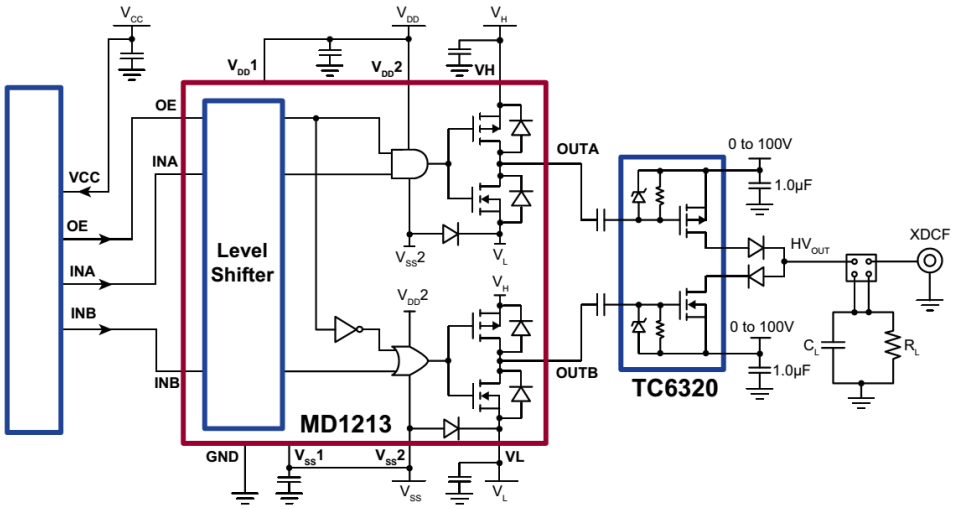

Figure 23: functional diagram of the circuit implementing MD1213 and TC6320 by Supertex.

IMPEDANCE MEASUREMENT CIRCUIT

The core of the BIST strategy lies in getting impedance data on the piezoelectric sensors, thus a review of impedance is in order. Impedance (Z) is generally defined as the total opposition a device or circuit presents to the flow of an alternating current (AC) at a given frequency, and is represented as a complex quantity which is graphically shown on a vector plane [Agilent, 2009]. The impedance is typically given in the rectangular form as resistance R, and reactance X, or polar format.

$$Z = R + jX = |Z|\angle\theta \tag{4.1}$$

Where $|Z|$ is the magnitude,

$$|Z| = \sqrt{R^2 + X^2} \tag{4.2}$$

and θ is the phase angle.

$$\theta = \tan^{-1}\left(\frac{X}{R}\right) \tag{4.3}$$

The reciprocal of Impedance is the admittance (Y),

$$\frac{1}{Z} = \frac{1}{R + jX} = Y = G + jB \tag{4.4}$$

where G is the conductance and B is the susceptance. Admittance may be more convenient to work with in some cases, such as parallel real and imaginary components, as shown below.

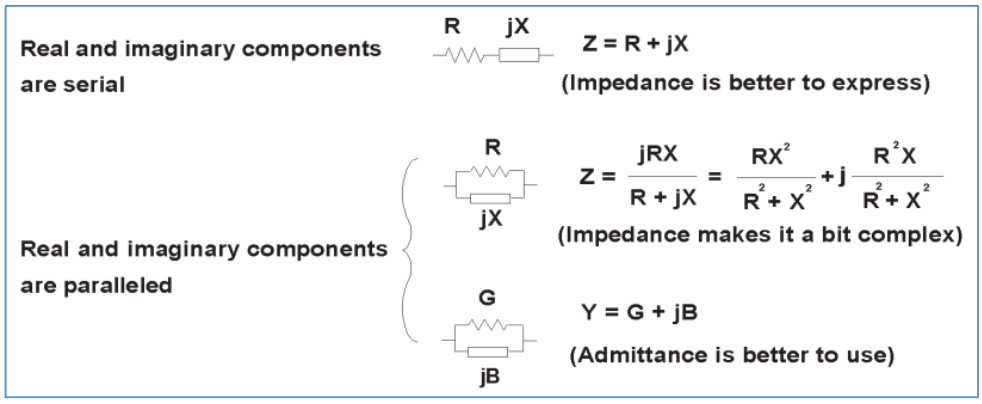

Figure 24: Expression of series and parallel combination of real and imaginary components [Agilent, 2009].

The reactance may be in the form of capacitance, X_c or inductance X_L

$$X_c = \frac{1}{\omega C} \tag{4.5}$$

$$X_L = \omega L \tag{4.6}$$

where the angular frequency is $\omega = 2\pi f$. The quality factor (Q) is a measure of the reactance purity and is defined as the ratio of the energy stored in a component to the energy dissipated by the component.

$$Q = \frac{X}{R} = \frac{B}{G} \tag{4.7}$$

The dissipation factor is defined as DF in this text to avoid confusion with other parameters. The dissipation factor is inversely proportional to the quality factor and may be defined by the tangent of the loss angle δ.

$$DF = \tan\delta = \frac{R}{X} = \frac{G}{B} \tag{4.8}$$

The loss angle is the complementary angle to the phase angle theta.

Analog Devices AD5933

The AD5933 is an impedance converter system on chip (SoC), with a frequency range up to 100kHz, and provides the real and imaginary components over an i^2c interface. Shown below is a block diagram for the AD5933.

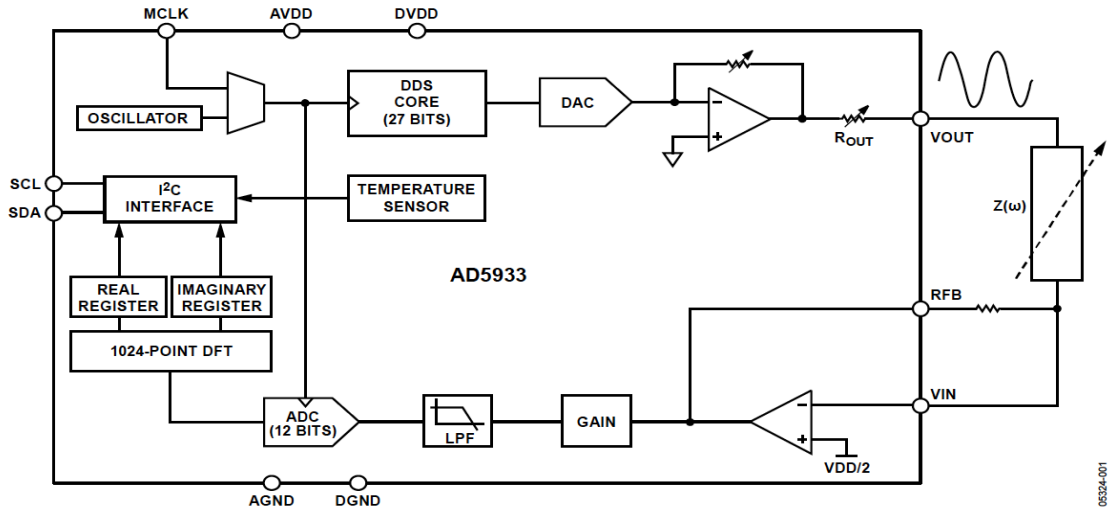

Figure 25: Functional block diagram of the AD5933 [Analog Device, 2013].

The AD5933 has a RAM register map to communicate commands to control operation, set parameters, read status and data. This allows the user to select the start frequency, frequency resolution, and the number of points in the frequency sweep. Additionally the peak-to-peak value of the sinusoidal output may be programmed to one of four possible values, shown below for 3.3V.

Range	Output Excitation Voltage Amplitude	Output DC Bias Level
1	1.98 V p-p	1.48 V
2	0.97 V p-p	0.76 V
3	383 mV p-p	0.31 V
4	198 mV p-p	0.173 V

Table 8: AD5933 output voltage values and respective output DC bias level for 3.3V.

The output excitation and DC bias levels are ratio metric with VDD.

$$Output\ excitation\ voltage\ for\ Range\ 1 = 1.98 \times \frac{5.0}{3.3} = 3V_{p-p}$$

$$Output\ DC\ bias\ voltage\ for\ Range\ 1 = 1.48 \times \frac{5.0}{3.3} = 2.24V_{p-p}$$

The excitation signal is generated by a 27-bit phase accumulator DDS core that offers a programmable frequency resolution down to 0.1Hz. Although the phase accumulator offers 27 bits of resolution only 24 bits are programmable since the start frequency register has the three most significant bits set to zero internally.

AD5933 Sweep Parameters

The start frequency is a 24-bit word that is programmed into the RAM at register address 0x82, 0x83, and 0x84. The start frequency code is given by the formula below.

$$Start\ frequency\ Code = \frac{Start\ frequency}{\frac{MCLK}{4}} \times 2^{27} \quad (4.9)$$

For example, if a start frequency of 30kHz is desired and the MCLK is 16MHz, then the code that needs to be programmed into the registers is 0x0F5C28. The Frequency Increment is a 24-bit word programmed into registers 0x85, 0x86, and 0x87, and the formula is given below.

$$Frequency\ Increment\ Code = \frac{Frequency\ Increment}{\frac{MCLK}{4}} \times 2^{27} \quad (4.10)$$

For a 16MHz MCLK and a desired frequency increment value of 10Hz, the code that needs to be programmed is 0x00014F. The Number of Increments (511max) is the number of frequency points in the sweep represented by a 9-bit word stored in registers 0x88 and 0x89. For example, if we wanted 401 frequency increments, then the frequency increment code would be 0x0191.

AD5933 Receive Description

The receive stage comprises of a current-to-voltage amplifier, followed by a programmable gain amplifier (PGA), antialiasing filter, and an ADC.

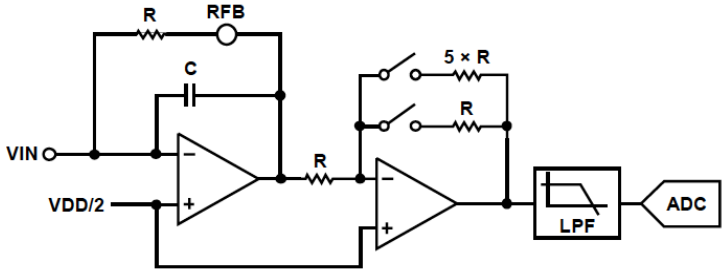

Figure 26: Receive stage of the AD5933. [Analog Devices, 2013]

The gain of the current-to-voltage amplifier is set by an external feedback resistor connected between pin 4 (RFB) and 5 (VIN). The gain of the PGA is digitally selected to

be 5 or 1 set by control register 0x80, bit D8. The signal is then low-ass filtered and presented to the input of the 12-bit, 1 MSPS ADC. The digital data from the ADC is passed directly to the AD5933 DSP core for the Discrete Fourier Transform (DFT).

A DFT is calculated for each frequency point in the sweep and is represented by the equation below.

$$X(f) = \sum_{n=0}^{1023} [x(n)(\cos n - j \sin n)] \tag{4.11}$$

The DFT parameters are defined in the table below.

X(f)	The power in the signal at the frequency point f.
x(n)	Output of the ADC
cos (n) sin (n)	Sampled test vector provided by the DDS core at the frequency point f.
n	Sample. The multiplication is accumulated over 1024 for each frequency point.

Table 9: AD5933 output voltage values and respective output DC bias level for 3.3V.

The result is stored in two 16-bit registers for the real and imaginary components in two's complement form. The first step towards calculating the impedance is to calculate the magnitude of the DFT real and imaginary components for each frequency point. This magnitude must be multiplied by the gain factor, which is calculated during system calibration, to obtain the impedance sensed at the VOUT and VIN pins. The impedance is then given by the equation below.

$$Impedance = \frac{1}{Gain\ Factor \times Magnitude} \tag{4.12}$$

AD5933 Performance Limitation Remedy

There are performance limitations associated with the AD5933 due to the output impedance of the transmit amplifier and the characteristics of the trans-impedance receive amplifier. A remedy is provided in application note CN-0217 [Analog Devices CN-0217], and is summarized in this section. The performance of the AD5933 may be improved and extended with external circuitry, as shown below.

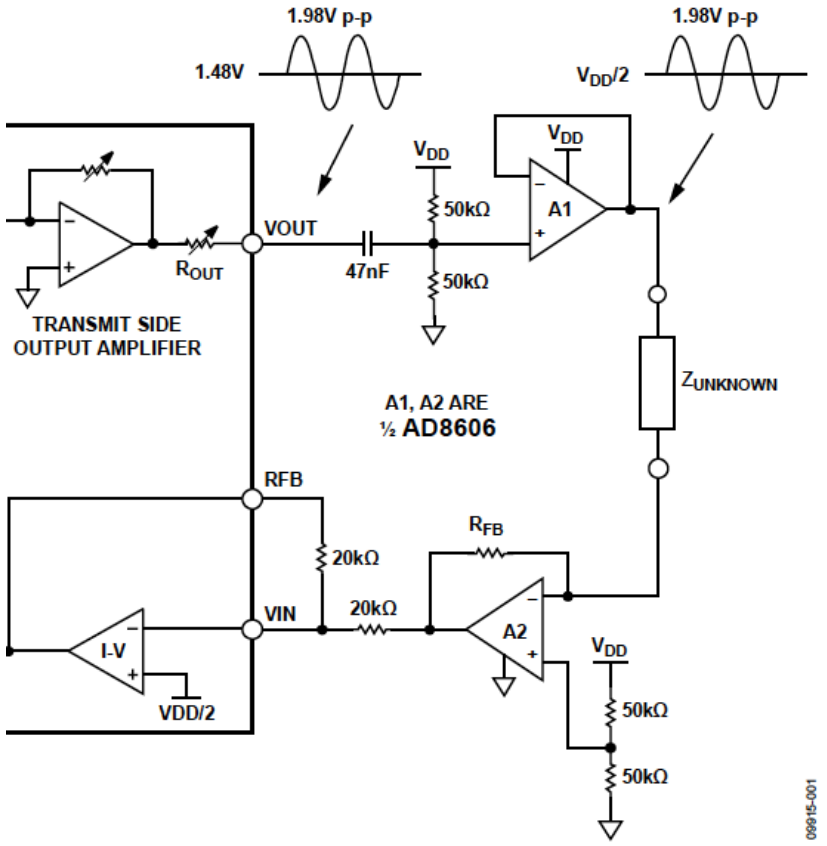

Figure 27: External circuits improving and extending the performance of AD5933 [Analog Devices 2013].

The output impedance affects the impedance measurement accuracy, especially in the low kilo-ohm range. Shown below is a table of the four possible output amplitudes and their respective Rout.

Range	Output Excitation Amplitude (V p-p)	Output Resistance (R_{OUT})
Range 1	1.98	200 Ω typical
Range 2	0.97	2.4 kΩ typical
Range 3	0.383	1.0 kΩ typical
Range 4	0.198	600 Ω typical

Table 10: AD5933 output voltage values and respective output DC bias level for 3.3V.

Adding a buffer to the transmit output will prevent the IC output impedance from affecting the unknown impedance. The buffer will need to have a low output impedance, and sufficient bandwidth.

Due to the variable output DC bias level of the integrated transmit amplifier, and the constant Vdd/2 offset of the trans-impedance receive amplifier, the opportunity exists for polarization of the impedance under test. This is fixed by adding a high-pass filter, given as 47nF, and a Vdd/2 voltage divider for constant offset as shown in the figure above. The receive side is improved with an external trans-impedance amplifier and matching Vdd/2 voltage divider. The external receive amplifier is chosen to have Lower bias current, lower offset voltage, and excellent CMRR to make the I-V conversion more accurate.

Chapter 5: Results and Analysis

Two different piezoelectric transducers are analyzed using the impedance resonance method. To create a baseline measurement, a calibrated impedance analyzer was used to make measurements over the various frequency bands of interest. Measurements are taken from 10kHz to 100kHz and then range is narrowed down to focus on a particular resonance. The measurements are repeated using the AD5933 and are compared to the baseline measurements.

IMPEDANCE MEASUREMENT WITH THE 4294A

The Agilent 4294A is a trusted device and was used for baseline measurements on two different transducers.

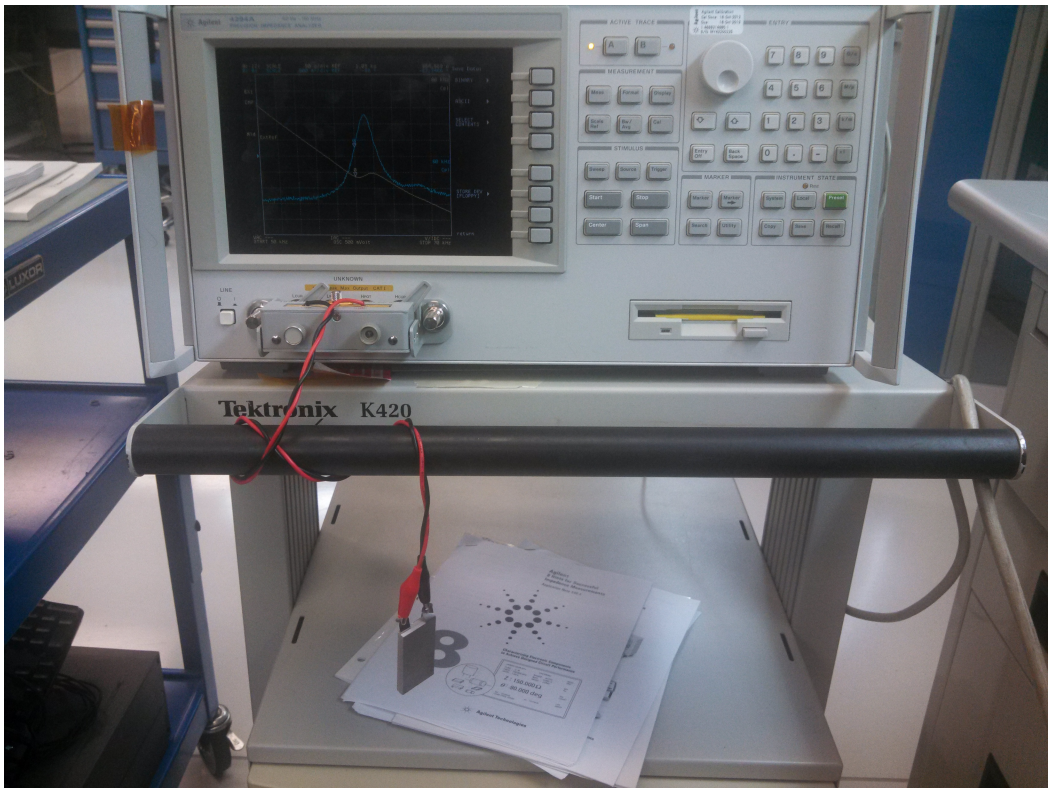

Figure 28: Picture of the 4294A impedance analyzer used for baseline measurements.

The measurement was performed by attaching the alligator clip leads to the transducer and inserting the wires on the other end into the kelvin plates of the impedance analyzer. All plots are taken with a signal strength of 500mV and 401 data points. Data is saved to a floppy disk in ASCII format and processed in MATLAB. Only the magnitude and phase data is saved from measurements and from these all other calculations are made.

Impedance Plots of Transducer 18a40b

Shown below is an impedance plot of transducer 18a40b from 10kHz to 200kHz. The plot shows a primary resonance at ~40kHz and a secondary resonance at ~165kHz.

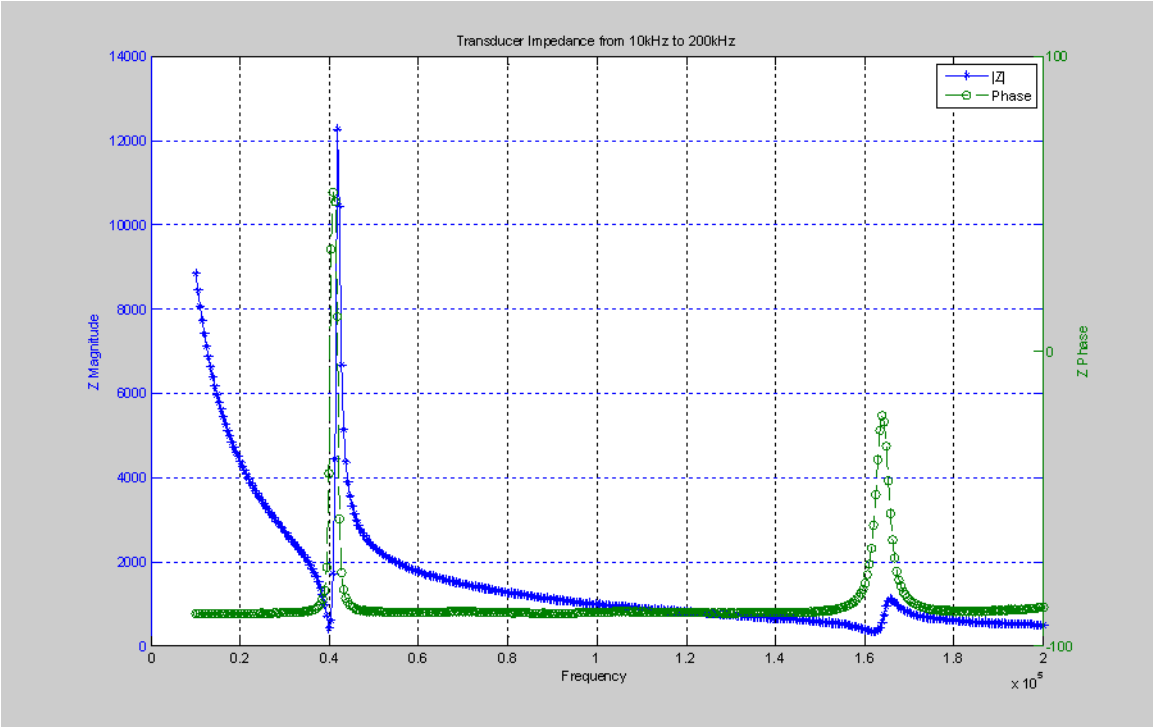

Figure 29: Transducer 18a40b Impedance data from 10kHz to 200kHz from 4294A impedance analyzer.

The plots below show the impedance magnitude and phase, and the real and imaginary components separately over the range of 10kHz to 100kHz.

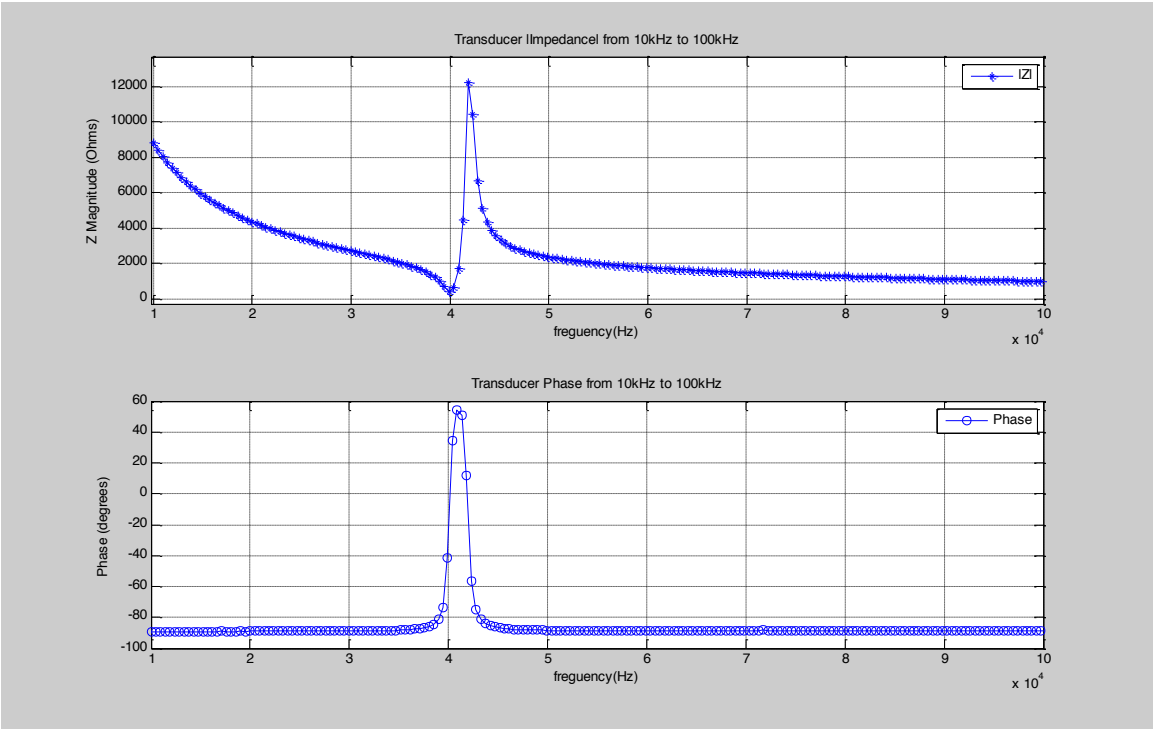

Figure 30: Transducer 18a40b Magnitude and Phase Impedance data from 10kHz to 100kHz from 4294A impedance analyzer.

Although the peaks appear well defined, the data points get rather sparse in the area of resonance.

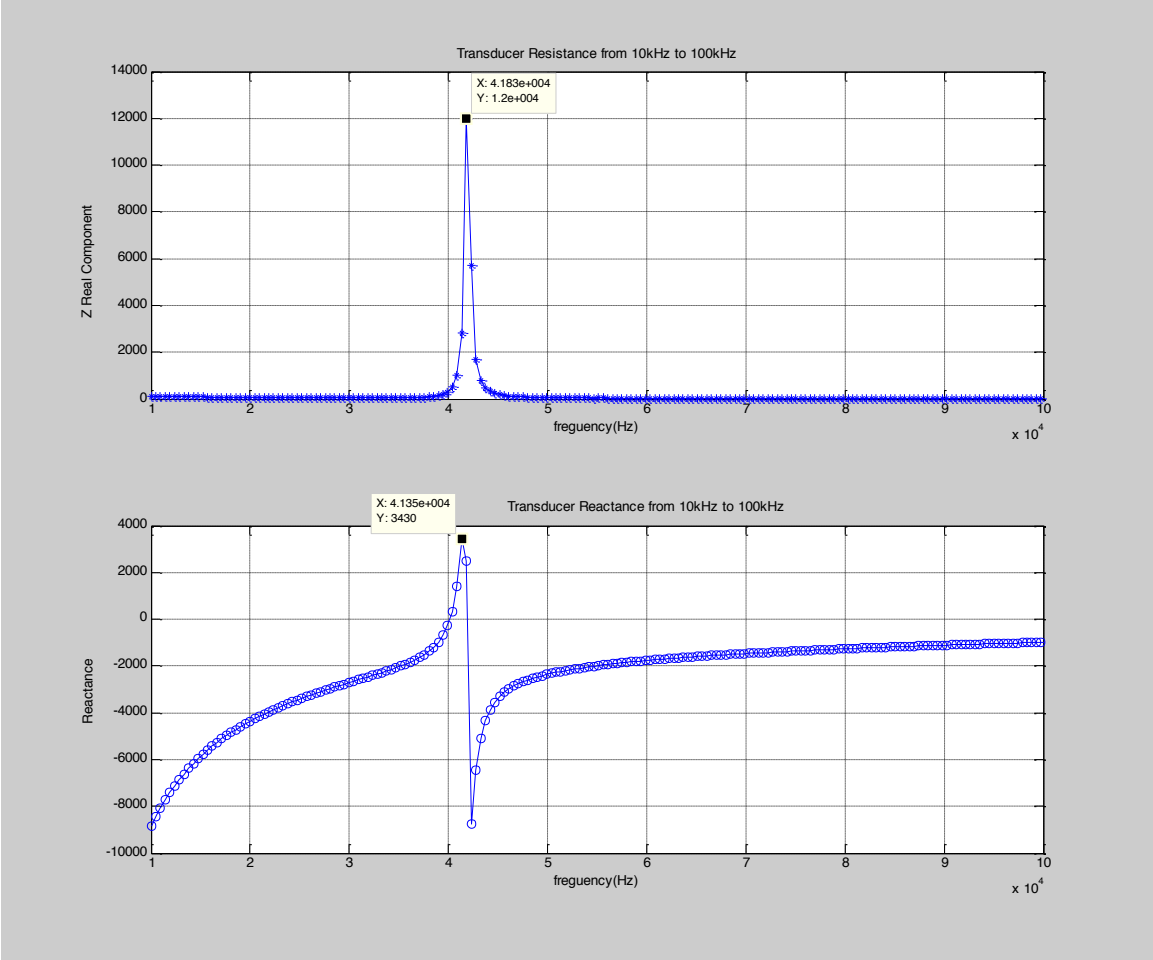

Figure 31: Transducer 18a40b Real and Imaginary Impedance data from 10kHz to 100kHz from 4294A impedance analyzer.

Once again, although the peaks appear well defined, the data points get rather sparse in the area of resonance. This makes it difficult when trying to generate an impedance circle plot since it utilizes the points in the area of resonance. Thus the with the same amount of data points, the frequency measurment range was further reduced to 36kHz to 46kHz, as shown below.

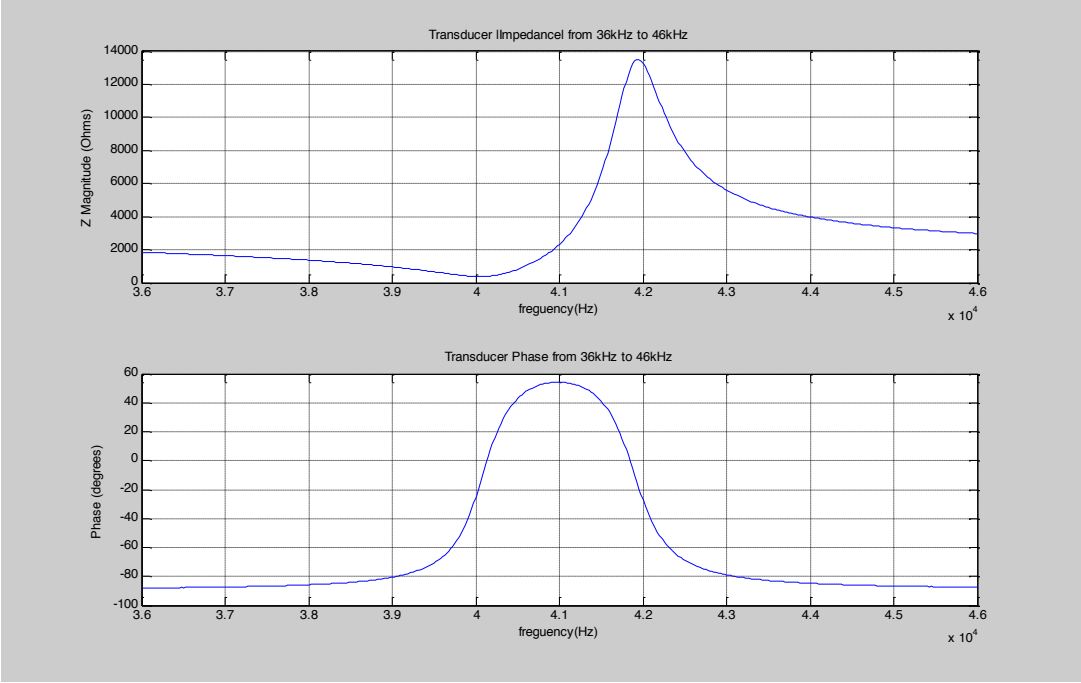

Figure 32: Transducer 18a40b |Z| and Phase Impedance data from 36kHz to 46kHz

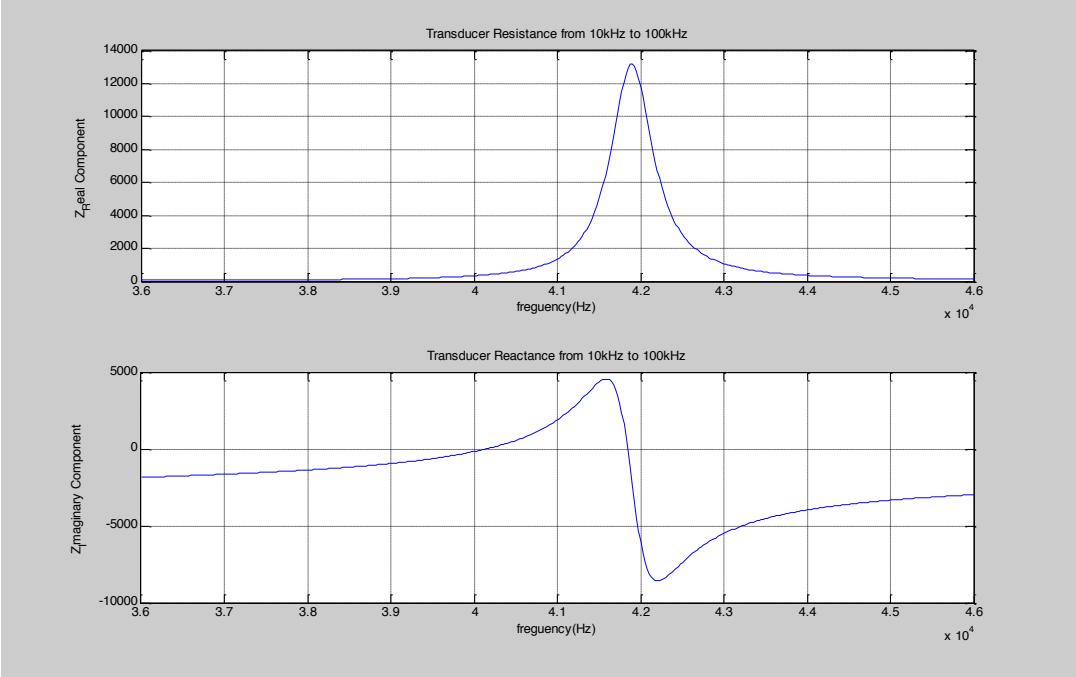

Figure 33: Transducer 18a40b Real and Imaginary Impedance data from 36kHz to 46kHz.

The range provides plenty of data point in the area of resonance for a nice impedance circle plot as shown below.

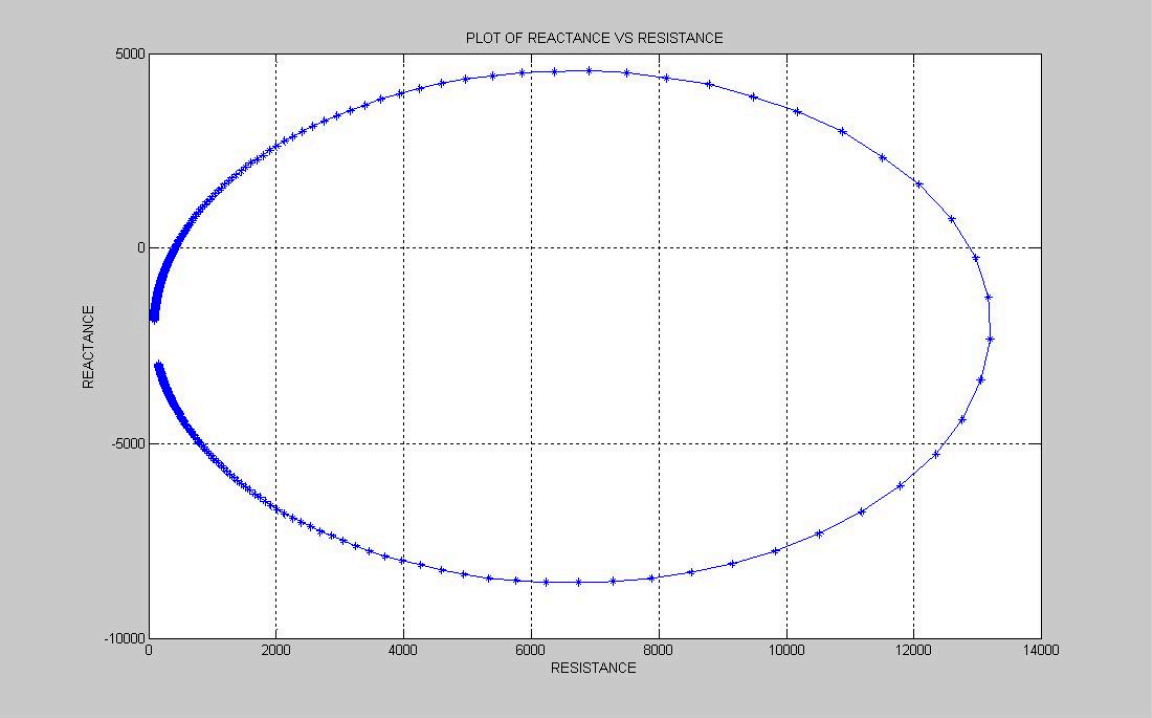

Figure 34: Transducer 18a40b Impedance Circle Plot data from 36kHz to 46kHz.

AD5933 IMPEDANCE MEASUREMENT CIRCUIT DATA

The impedance measurements obtained using the AD5933 were based on the demo board and GUI provide to interface the demo board via USB. The software allowed communication to the AD5933 so that the control registers may be programmed, sweep parameters set by the user. The software was used for data display and provided an option to download to PC, where MATLAB was used for processing.

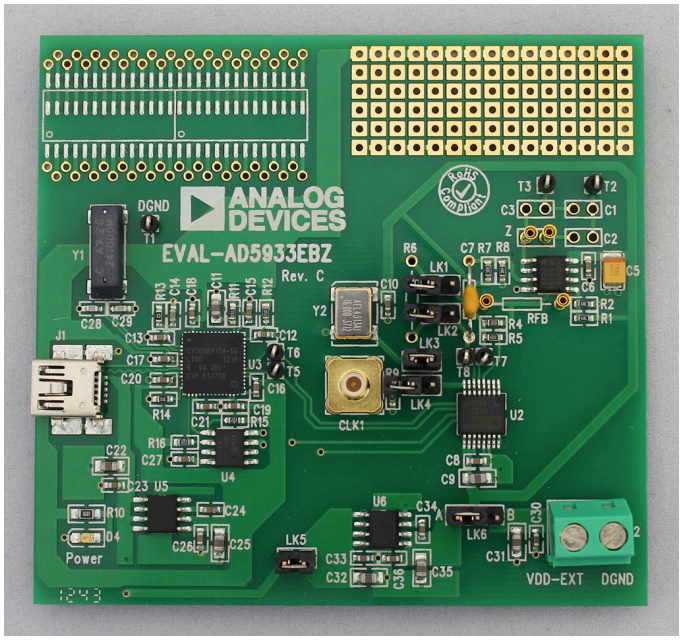

Figure 35: Analog devices AD5933 demo board.

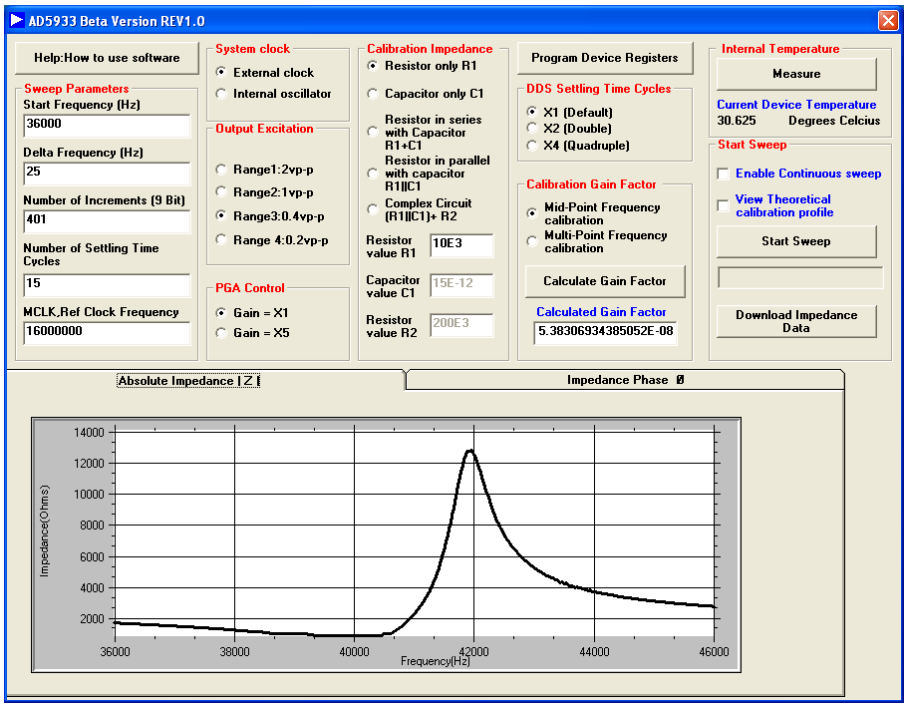

Figure 36: Analog devices AD5933 demo board software GUI.

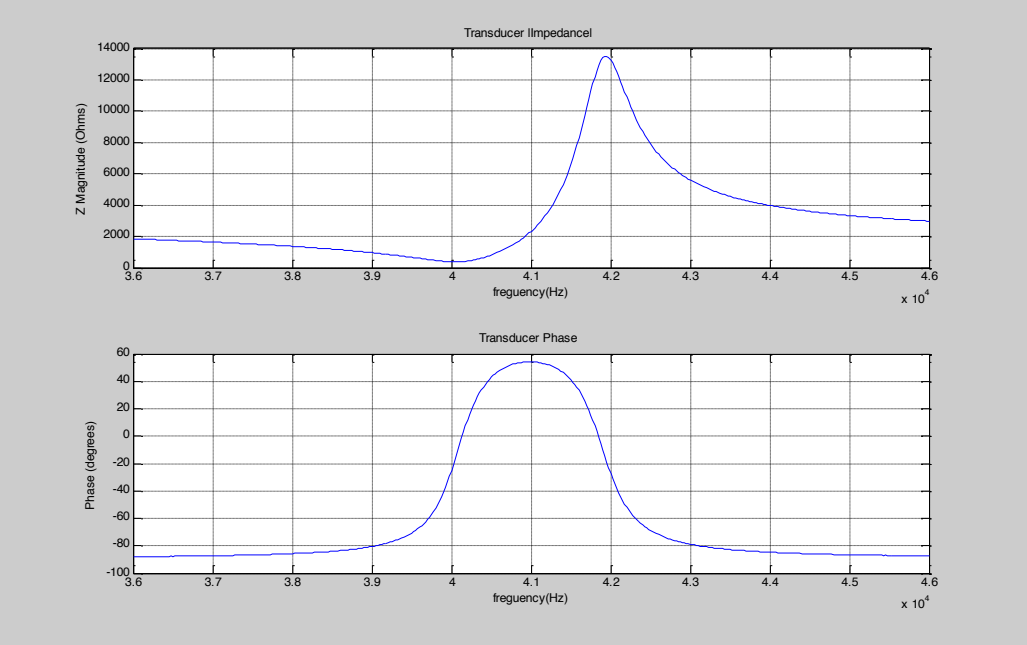

Figure 37: Transducer 18a40b |Z| and Phase Impedance data from AD5933

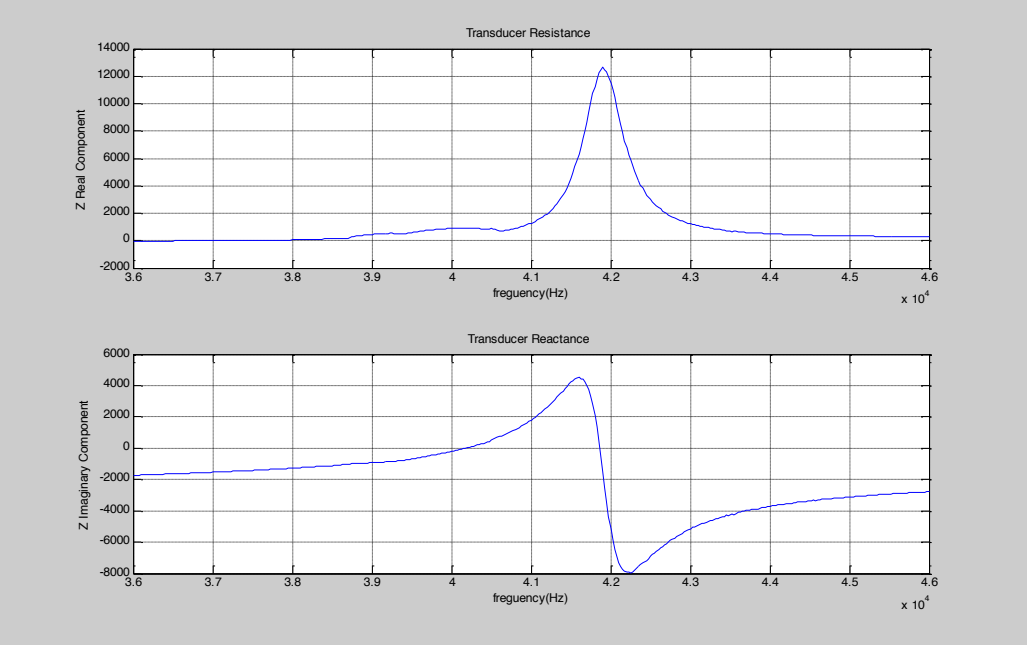

Figure 38: Transducer 18a40b Real and Imaginary Impedance data from AD5933

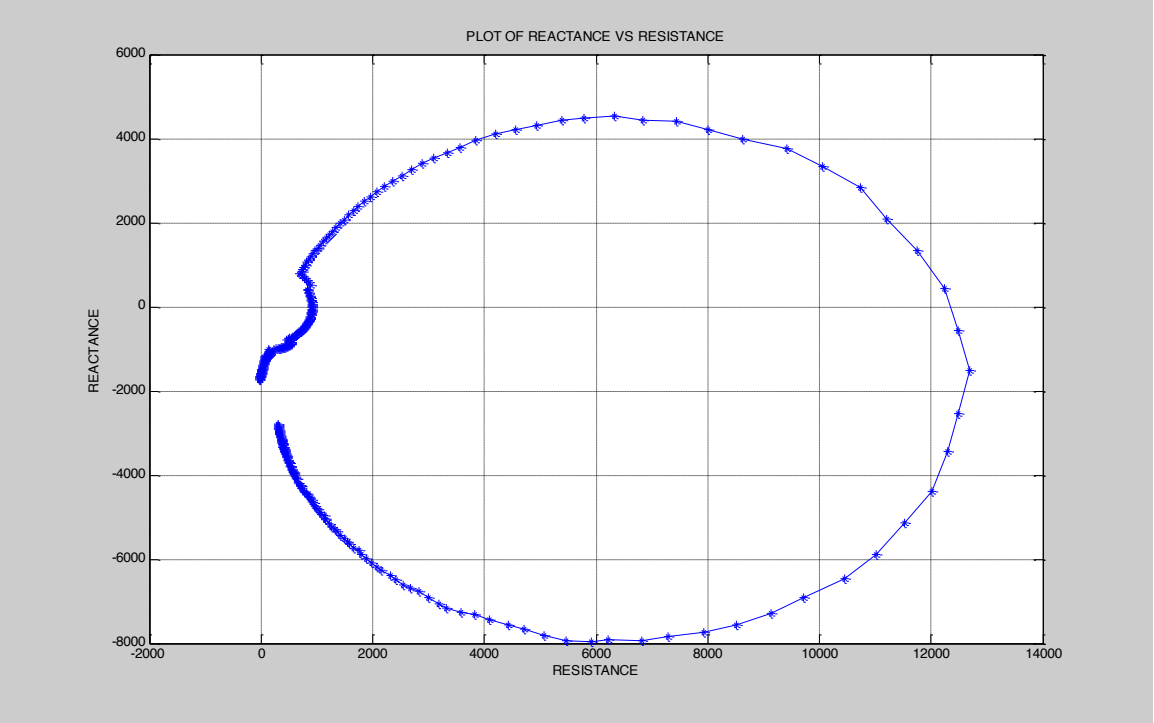

Figure 39: Transducer 18a40b Impedance Circle Plot data from AD5933.

There is good agreement between the AD5933 data and the baseline data from the 4294. There is a hiccup early in the early frequency data points which appears as a dent in the circle plot that may be attributed to the settle time and requires further investigation.

Chapter 6: Conclusion

As can be seen from the plots in the data section, there is good agreement between the measured impedance data from the AD5933 and the baseline data from the Agilent 4294A impedance analyzer. This will allow accurate piezoelectric transducer impedance data in the area of resonance to be obtained in an embedded environment. The theory behind and practice of measuring ceramic piezoelectric transducer data is well established and it has been shown that carefully obtained impedance data may be used as a basis to calculate piezoelectric coefficients. Although there are non-idealities that may cause inaccurate calculations of the true piezoelectric effect of the ceramic based on impedance data, the relative measurements may still be used to provide indication of transducer deterioration over time.

The scope of this report was limited to a review of the ceramic piezoelectric sensor physics and impedance analysis characterization; the data shows promise for additional applications. The next steps will be to realize an ultrasound transmit and receive circuit, and correlate deteriorating ultrasonic signal reception with their impedance curves. Additionally an embedded impedance measurement circuit that works for frequency ranges above 100kHz will allow more detailed analysis.

References

Agilent Technologies, Inc. 2009. Agilent Impedance Measurement Handbook, A guide to measurement technology and techniques, 4th edition.

Analog devices, 2005-2013. AD5933 datasheet. http://www.analog.com/static/imported-files/data_sheets/AD5933.pdf

APC International, LTD (formerly American Piezo Ceramics Inc.). 2011. Piezoelectric Ceramics: Principles and Applications.

Azhari, H. 2010. Basics of Biomedical Ultrasound for Engineers. John wiley & Sons, Inc.

Butterworth, S. 1915. On Electrically-maintained Vibrations. Proc. Phys. Soc. (London), Vol. 27.

Cady, W, G. 1946. Piezoelectricity.

Frandon, J. 2009. The Complete Guide to Rocks & Minerals. Hermes House.

Galliere, J.-M., Papet, P., Latorre, Laurent. 2007. A Unified Electrical SPICE Model for Piezoelectric Transducers. IEEE.

Guan, M., Liao, W.-H. 2004. Studies on the Circuit Models of Piezoelectric Ceramics. International Conference on Information Acquisition, p. 26-31.

Hyne, N.J. 2012. Nontechnical Guide to Petroleum Geology, Exploration, Drilling & Production. PennWell Corporation.

IEEE std 177. 1966. Standard Definitions and Methods of Measurement for Piezoelectric Vibrators. IEEE New York.

IEEE/ANSI Std 176. 1987. IEEE Standard on Piezoelectricity. IEEE, New York.

IRE 1957. IRE Standards on Piezoelectric Crystals- The Piezoelectric Vibrator: Definitions and Metods of Measurement. IRE, New York.

IRE 1961. IRE Standards on Piezoelectric Crystals: Measurements of Piezoelectric Ceramics. IEEE, New York.

Jaffe, B., Cook Jr., W. R., and Jaffe, H. 1971. Piezoelectric Ceramics, Academic Press London and New York.

Kim, J., Grisso, B.L., Kim, J.K., Ha, D.S., Inman, D. J. 2008. Electrical Modeling of Piezoelectric Ceramics for Analysis and Evaluation of Sensory Systems. IEEE Sensors Applications Symposium. Atlanta, Georgia.

Kwok, K.W., Chan, H.L.W., Choy, L.C. 1997. Evaluation of the Material Parameters of Piezoelectric Materials by Various Methods. IEEE Transactions on Ultrasonics, Ferroelectrics, and Frequency Control, Vol.44, No.4.

Krimholtz, R., Leedom, D.A., Matthaei, G.L. 1970. New Equivalent Circuit for Elementary Piezoelectric Transducers. Electron Letters, Electron. Lett. 6, p. 398-399.

Lee, S.J., Sohn, H. 2010. Piezoelectric Transducer Self-Diagnostic Under Changing Environmental and Structural Conditions. IEEE Transactions on Ultrasonics, Ferroelectrics, and Frequency Control, Vol.57, No.9.

Lee, S.J., Sohn, H., Hong, J.-W. 2010. Time Reversal Based Piezoelectric Transducer Self-diagnosis Under Varying Temperature. Journel of Nondestructive Evaluation 29: 75-91. Springer Science+ Business Media, LLC.

Redwood, M. 1961. Transient Performance of a PiezoelectricTransducer. Journal of the Acoustical Society of America, 33, p.527-536.

Safari, A., Akdogan, E. K. 2008. Piezoelectric and Acoustic Materials for Transducer Applications. Springer.

Sherrit, S., Wiederick, H.D., Mukherjee, B.K. and Sayer, M. 1997. An Accurate Equivalent Circuit for the Unloaded Piezoelectric Vibrator in the Thickness Mode. Journal of Physics D: Applied Physics, vol. 30, no. 16, p. 2354-2363.

Sherrit, S., Wiederick, H. D., Mukherjee, B. K. 1992. Non-iterative evaluation of the real and imaginary material constants of piezo-electric resonators. Ferroelectrics, vol. 134, p. 111-119.

Sherrit, S. Leary, S.P., Dolgin, B.P., Bar-Cohen, Y. 1999. Comparison of the Mason and KLM Equivalent Circuits for Piezoelectric Resonators in the Thickness Mode. IEEE Ultrasonics Symposium.

Smits, J. G. 1976. Iterative method for accurate determination of the real and imaginary parts of the materials coefficients of piezo-electric ceramics. IEEE Trans. Sonics Ultrason., vol. SU-23, p.393-402.

Voigt, W. 1910. Lehrbuch der Kristallphysik: (mit Ausschluss der Kristalloptik). B. G. Teubner in Leipzig.